

Loughborough University  
Wolfson School of Mechanical, Electrical  
and Manufacturing Engineering

# **Recycling inert gases for plasma-assisted carbon dioxide splitting using a split-ring resonator**

Prateep Ganesh Kasinathan

1<sup>st</sup> March 2023



# Contents

<b>1</b>	<b>Introduction</b>	<b>1</b>
1.1	Motivation . . . . .	1
1.2	Novelty . . . . .	2
<b>2</b>	<b>Plasma Overview</b>	<b>4</b>
2.1	Paschen's Law . . . . .	4
2.2	DC Discharge . . . . .	6
2.2.1	DC Discharge Sources . . . . .	9
2.3	AC Discharge . . . . .	12
2.3.1	AC Discharge Sources . . . . .	14
<b>3</b>	<b>Carbon Dioxide Splitting</b>	<b>21</b>
3.1	Traditional Process . . . . .	21
3.2	Plasma-assisted $CO_2$ Splitting . . . . .	24
<b>4</b>	<b>Split Ring Resonator</b>	<b>26</b>
4.1	Overview . . . . .	27

4.2 Production . . . . .	29
4.2.1 Simulations . . . . .	29
4.2.2 Design . . . . .	34
4.3 Testing . . . . .	38
4.3.1 Scattering Parameters . . . . .	38
4.3.2 Experimental Setup . . . . .	39
4.3.3 Plasma performance . . . . .	41
<b>5 Epoxidation Process</b>	<b>45</b>
<b>6 Gas recirculation</b>	<b>46</b>
<b>7 Conclusion</b>	<b>47</b>
<b>A Particle-in-Cell Simulations</b>	<b>48</b>
A.1 Particle Mover . . . . .	50
A.2 Charge and Current Deposition . . . . .	53
A.3 Field Solver . . . . .	54
A.4 Field Interpolation . . . . .	57
A.5 Monte-Carlo Collisions . . . . .	58
<b>B XOOPIIC</b>	<b>60</b>
B.1 Overview . . . . .	60
B.1.1 Remote Server . . . . .	61

B.1.2	Input Files . . . . .	62
B.2	Improvements . . . . .	63
B.2.1	Motivation . . . . .	63
B.2.2	Methodology . . . . .	65
B.2.3	Validation . . . . .	70
B.2.4	Future Work . . . . .	76
	<b>Bibliography</b>	<b>76</b>



# List of Tables

4.1	Simulation parameters of SRR in XOPIC.	29
A.1	Determining the type of collision based on the value of $R$ [66].	59
B.1	Circuit boundary variables for cartesian geometry.	69
B.2	Circuit boundary variables for cylindrical geometry.	70
B.3	Parameters for test case of Circuit boundary without particles.	71
B.4	Parameters for test case of Circuit boundary with particles.	74



# List of Figures

1.1	Global greenhouse gas emissions by sector [3]. . . . .	2
2.1	Paschen curve for Helium, Neon, Argon, Hydrogen, and Nitrogen gases [6]. . . . .	6
2.2	Circuit diagram with a source voltage ( $V_s$ ) and variable resistor ( $R$ ) to control the current through a discharge region ( $C$ to $A$ ) [7]. . . . .	7
2.3	Depiction of the current-voltage relationship across three discharge regions [8]. . . . .	7
2.4	Schematic highlighting the regions present in a DC glow discharge [9]. The cathode is on the left and the grounded anode is on the right. (CDS is the cathode dark space, NG is the negative glow, and AZ is the anode dark space. . . . .	9
2.5	A DC plasma from molecular emission detector on chip [10]. . . . .	10
2.6	A simplified illustration of a hollow cathode design [12]. . . . .	11
2.7	A comparison of the voltage vs current curve for a hollow cathode geometry (solid line) and a typical parallel plate geometry (dashed line)[14]. . . . .	12
2.8	Paschen curve for AC discharge across various frequencies [24]. . . . .	14
2.9	Illustration of a capacitively coupled plasma (CCP) experimental setup [26]. . . . .	15
2.10	Cycle averaged electron temperature in a CCP reactor [27]. . . . .	15
2.11	Schematic of inductively coupled plasma (ICP) torches [30]. . . . .	16

2.12 Comparison of plasma parameters between CCP and ICP reactor [31]. The two left most graphs (a, c) are the results from a CCP reactor, while the two right most graphs (b, d) are the results of the ICP reactor. The top two graphs (a, b) show the radial distribution of electron temperatures for a CCP and ICP reactor respectively. The bottom two graphs (c, d) show the distribution of electron density for a CCP and ICP reactor respectively. . . . .	17
2.13 Examples of different Dielectric Barrier Discharge (DBD) designs [34]. The left most (a) and right most (c) drawings show at least one dielectric on the electrodes, while the middle (b) illustrates a dielectric in the discharge gap, but not touching the electrodes. . . . .	18
2.14 Schematic of a surface wave discharge plasma source [37]. . . . .	19
2.15 Schematic of an electron cyclotron resonance plasma source [37]. . . . .	19
2.16 Examples of different types of microstrip plasma sources [15]. The top three designs (a, b, c) are linear microstrip resonators, while (d) shows a microstrip split-ring resonator, and (e) illustrates a coaxial resonator. . . . .	20
3.1 Gibbs free energy of formation for different chemicals based on data from the NIST database. [42] . . . . .	22
3.2 Thermal conversion and energy efficiency of CO <sub>2</sub> splitting as a function of temperature. [43] . . . . .	22
3.3 Schematic of microwave reactors for CO <sub>2</sub> splitting. [43] . . . . .	24
4.1 Schematic (left) and photo (right) of SRR [50]. . . . .	27
4.2 A cross section comparison of SRR simulation domain without a hole (a) and with hole (b) in gap. . . . .	30
4.4 Time series plot of number of electrons across different discharge gaps. . . . .	32

4.6	PCB schematic of SRR panels in the KiCad software suite. . . . .	36
4.7	SRR gap designs with multiple holes (a, c) versus single holes (b, d). The designs in the lower two subfigures (c, d) have the presence of ‘finger-like’ copper pours next to the holes. . . . .	37
4.8	Reflection coefficient ( $S_{11}$ ) of SRR in dB. . . . .	39
4.9	Schematic of experimental setup. . . . .	40
4.10	Photograph of plasma discharge in the gap of the SRR. . . . .	41
4.11	Reflection power of SRR when connected to the setup in mW. . . . .	42
4.12	Ignition power of SSR, in mW, across a pressure range of 5 Torr to 850 Torr. . .	43
A.1	Process flow of PIC simulations. . . . .	49
A.2	Illustration of forward-difference and central-difference form [58]. . . . .	51
A.3	Visualisation of velocity rotation from the Boris algorithm [59]. . . . .	52
A.4	Interpolation from the grid to the particles [61]. . . . .	53
A.5	Illustration of ADI method [63]. . . . .	56
A.6	Addition of null collision to produce a constant collision frequency across all energies [66]. . . . .	59
B.1	Illustration of circuit boundary. . . . .	64
B.2	Voltage-current relationship of circuit boundary. . . . .	65
B.3	Illustration of a circuit boundary along a fixed grid. . . . .	66
B.4	Illustration of test case for Circuit boundary without particles. . . . .	71
B.5	Comparison between the analytical solution and XOOPIIC, where $\Delta t = 10$ ps. .	72

B.6 Comparison between the analytical solution and XOOPIIC, where $\Delta t = 1$ ns. . . . .	72
B.7 Comparison of the error from XOOPIIC when $\Delta t = 10$ ps and $\Delta t = 1$ ns. . . . .	73
B.8 Illustration of test case for Circuit boundary without particles. . . . . . . . . . .	73
B.9 Illustration of test case for Circuit boundary without particles. . . . . . . . . . .	76

# Chapter 1

## Introduction

Anthropogenic climate change is a real problem and has been stated as “a threat to human well-being and the health of the planet” by the Intergovernmental Panel on Climate Change (IPCC) [1]. The driving force behind climate change has to do with the emissions of green house gases into the atmosphere. According to data from the United States Environmental Protection Agency, carbon dioxide ( $\text{CO}_2$ ) accounts for nearly three quarters of those greenhouse emissions [2]. A breakdown of emissions by sector can be seen in figure 1.1.

As seen in figure 1.1, global greenhouse emissions come from a variety of sources and processes. Hence, simply focusing efforts in areas such as transport or electricity generation is insufficient. Eliminating our dependance on fossil fuels by switching to renewables or driving electric cars is a start, but in order to achieve net-zero emissions, there needs to be innovations across various other sectors. Currently, there is no one solution to climate change.

### 1.1 Motivation

Now, supposing that we have successfully decarbonised the economy, there will always be industrial processes that produce  $\text{CO}_2$  as a byproduct. The quintessential example of this is the manufacturing of concrete, where the  $\text{CO}_2$  is released from a chemical process due to

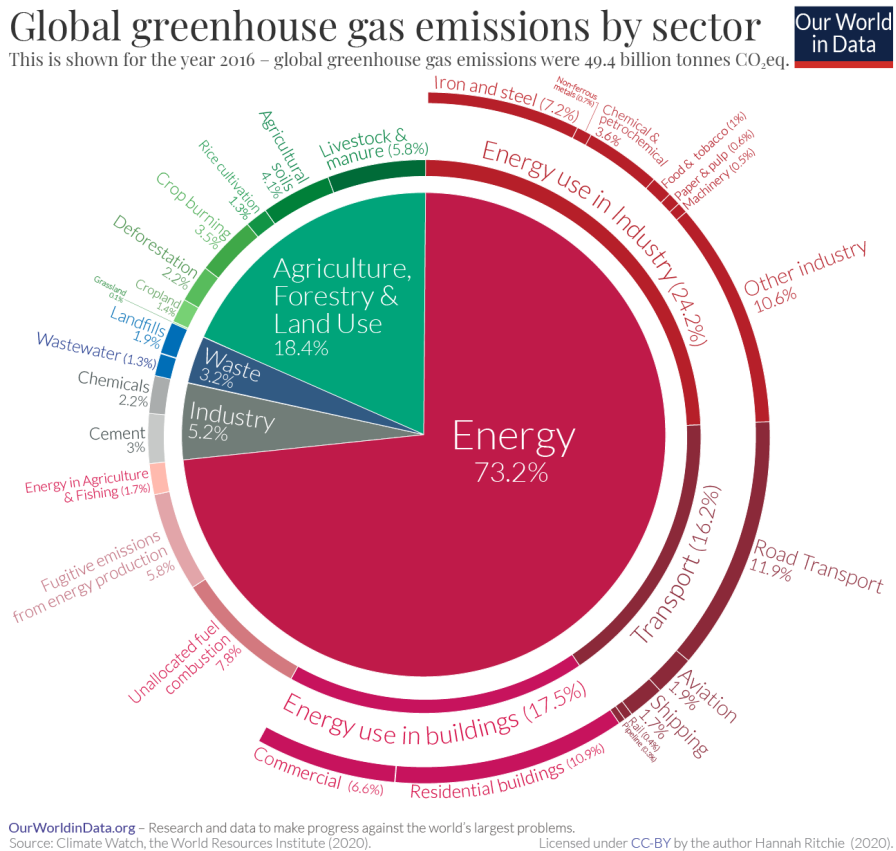


Figure 1.1: Global greenhouse gas emissions by sector [3].

the conversion of calcium carbonate ( $\text{CaCO}_3$ ) to calcium oxide ( $\text{CaO}$ ), rather than through combustion. As such it would be useful to capture this  $\text{CO}_2$  and potentially reuse it in other manufacturing processes.

There have many different approaches in the literature, with recent examples including generating synthetic fuels using electrochemical  $\text{CO}_2$  recycling [4] and using algae to convert  $\text{CO}_2$  into carbon fibre [5]. This report will specifically focus on the area of carbon conversion via  $\text{CO}_2$  splitting; specifically, plasma-assisted  $\text{CO}_2$  splitting.

## 1.2 Novelty

Plasma-assisted  $\text{CO}_2$  splitting is a relatively new technology that could be used for the process carbon conversion. In order to generate and sustain this plasma, inert feed gases (typically argon or helium) are oftentimes required. While the use of these feed gases are perfectly viable

in a research laboratory setting, when it comes to scaling the process to an industrial level, the costs associated become untenable.

The novelty with this project is to asses the viability of a plasma driven carbon utilisation process that recirculates the feed gas, reducing the cost associated with the use of inert gases. This would require a control system to maintain the pressure of the feed gas as there will inevitably be some losses. It would also require the filtration of any waste products produced from the CO<sub>2</sub> splitting process and subsequent chemical reactions.

The rest of this report is structured as follows. A introduction of plasma discharges can be found in chapter 2. Chapter 3 goes on to provide an overview of the CO<sub>2</sub> splitting process. Then, chapter 4 provides a description of the process to design and develop the plasma reactor used for this project, along with some basic tests using only Helium gas. CO<sub>2</sub> gas is then introduced to the plasma reactor in chapter 5, where the results from the CO<sub>2</sub> splitting process can be found. Chapter 6 goes on to describe the mechanism of waste filtration and feed gas recirculation. Finally, the results of this report are discussed in the conclusion.

# Chapter 2

## Plasma Overview

Plasma is a fundamental state of matter, along with solid, liquid, and gas. It has similar characteristics to gases, where it is compressible and does not conform to a specific shape; however the key difference is that plasmas are highly electrically conductive, even capable of producing their own magnetic field. This is because plasmas contain a large number of positive ions that interact in a ‘sea’ of free-moving electrons.

There are two primary methods to generate plasma. The first is via extreme heating of a gas whereby the electrons gain sufficient energy to escape the electromagnetic force of the nucleus. The most obvious example of this is in stars where the gases within reach temperatures millions of degrees Kelvin, giving rise to nuclear fusion. The other method, which is the main focus of this report, is the exposure of a gas to a large electric field. This in turn ignites the plasma in a process described in the rest of this chapter. An everyday example of this is lightning, where charges build up between the clouds and the ground, which in turn causes the potential difference between the two to grow until the air in between breaks down.

### 2.1 Paschen’s Law

The voltage necessary to break down a gas is given by Paschen’s law. It states that the breakdown voltage is a function of two parameters [6]: the pressure of the gas and the distance

between the electrodes (referred to as the gap length). Specifically, the breakdown voltage is given by the product of these two parameters.

In order for breakdown to occur, there needs to be a small number of electrons already present in the gas. This can be caused internally by a smaller number of already excited gas molecules, or externally by highly energetic cosmic rays entering the gas chamber. Then by applying a voltage, these electrons gain energy creating other electrons via ionising collisions. When more electrons are generated from the collisions than are lost, an avalanche is created, which causes the gas breakdown.

The breakdown voltage can be expressed by the following equation [6]:

$$V_B = \frac{Bpd}{\ln(Apd) - \ln[\ln(1 - \frac{1}{\gamma_{se}})]} \quad (2.1)$$

where  $V_B$  is the breakdown voltage,  $p$  is the pressure of the gas,  $d$  is the gap length,  $\gamma_{se}$  is the coefficient for secondary-electron emission (explained in section 2.1.2), and  $A$  and  $B$  are constants for a given gas that are determined experimentally.

However it is much easier to understand Paschen's law pictorially. Figure 2.1 illustrates the voltage breakdown curves for various gases. Each curve is slightly different, however all of them do exhibit a convex shape. Supposing if:

- **The gap length remains constant.** Starting with a large pressure, the mean free path of an electron within the gas is quite short, meaning it does not have sufficient time in between collisions for it to gain enough energy to cause an ionising collision with the neutral gas. As the pressure is then reduced, the mean free path increases, making it easier for the electrons to gain sufficient energy to undergo ionising collisions; until a certain critical pressure that is (typically a  $pd$  of approximately 1 to 10 Torr cm). Beyond this, decreasing the pressure further causes the mean free path of the electron lengthen to a point that is comparable to the gap length, therefore this decreases the likelihood of an electron colliding with a neutral gas particle and the breakdown voltage increases.

- **The pressure remains constant.** When the gap length is very small, electrons are accelerated by a large electric field but are collected by the electrodes without undergoing collisions with the background gas. Increasing this gap length to a certain point gives the electrons the opportunity to collide with the background gas, producing ionising collisions. However, as the gap length continues to be increased, the strength of the electric field between the electrodes decreases, hence the electrons gain less energy between the collisions resulting in fewer ionising collisions with the background gas.

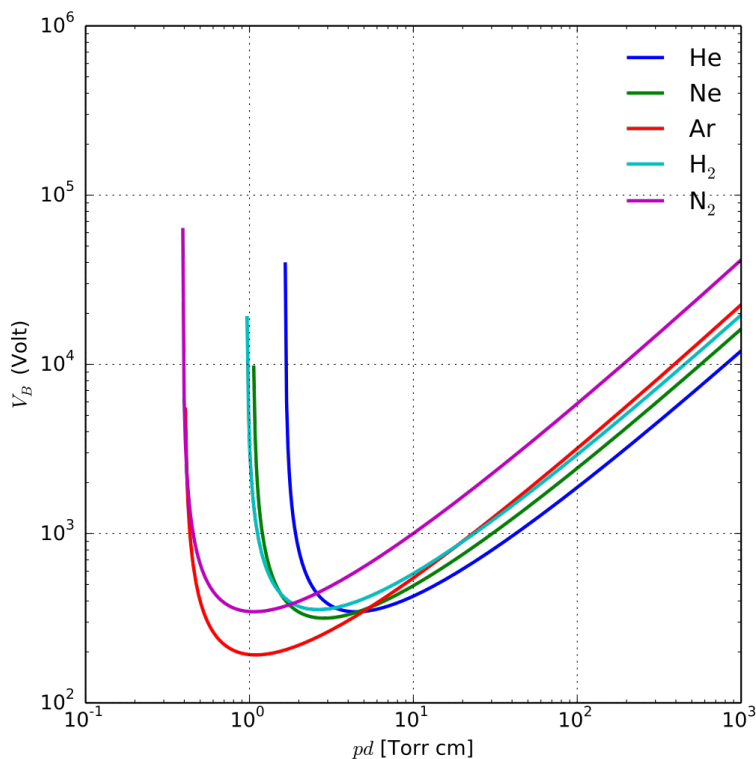


Figure 2.1: Paschen curve for Helium, Neon, Argon, Hydrogen, and Nitrogen gases [6].

## 2.2 DC Discharge

Consider a circuit as seen in figure 2.2. Two parallel electrodes with a DC voltage applied, and a neutral gas contained within a chamber. As the resistance of the variable resistor is decreased, which in turn increases the current through the plasma, one would observe three distinct discharge regions [7], observed in figure 2.3.

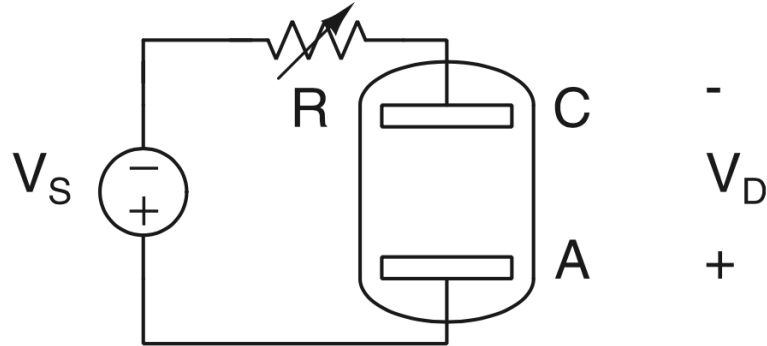


Figure 2.2: Circuit diagram with a source voltage ( $V_s$ ) and variable resistor ( $R$ ) to control the current through a discharge region ( $C$  to  $A$ ) [7].

The first, is the dark discharge (or sometime referred to as the Townsend discharge) region. Initially, the voltage between the electrodes builds up as the only current through the plasma is caused by pre-existing electrons, say from cosmic radiation; however this current quickly saturates (seen from region A-B in figure 2.3). Then, once the electrons gain sufficient energy, they begin colliding with the background gas to produce additional electrons in a process called the *Townsend avalanche* (seen from region B-D in figure 2.3). Once this avalanche is self-sustaining, the voltage breakdown of the gas is reached (at point D in figure 2.3).

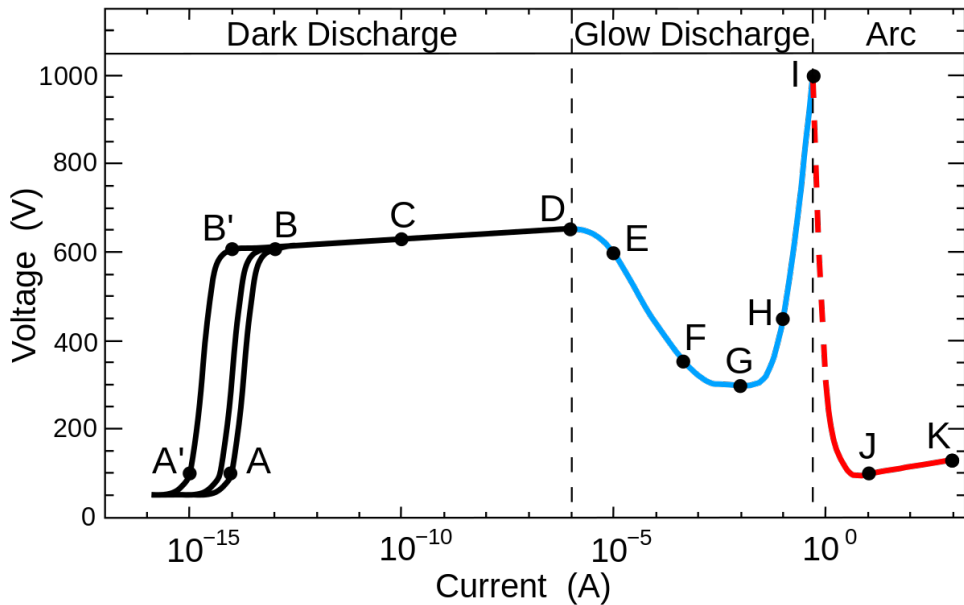


Figure 2.3: Depiction of the current-voltage relationship across three discharge regions [8].

After the breakdown, the plasma is said to be in a glow discharge region. Here, the voltage across the plasma decreases since a transition from a gas to plasma state causes a decrease in

resistance, implying that the ionisation process from the avalanche is more efficient (seen from region D-G in figure 2.3). This efficiency stems from the fact that the electrons are generated by a secondary means in addition to the standard Townsend avalanche. This process is called the secondary emission of electrons, which is caused by the energetic collisions of ions and metastables with the surface of the cathode. These *secondary-electrons* are then accelerated by the electric field and cause further Townsend avalanches.

At first, ion bombardment on the surface of the cathode is non-uniform but as the current generated from this increases, it eventually stabilises and the distribution of the plasma (and thus the ions) across the cathode become more uniform. This is referred to as *subnormal glow* and *normal glow* respectively. As the current is increased further, ion bombardment across the cathode becomes saturated as it covers the entire surface of the cathode (seen from region G-I in figure 2.3). This is referred to as *abnormal glow*, and increasing the current further causes the glow discharge to become an arc (at point I in figure 2.3).

In the arc discharge region, the ion bombardment onto the cathode causes the cathode to heat up to a point where electrons are generated via thermionic emission. This significantly reduces the resistance of the plasma, causing a very large drop of the voltage (seen from region I-J in figure 2.3).

For the purposes of this project, the arc discharge region will be avoided. The reason being, operating under arc conditions increases the electrode sputtering rate. *Sputtering* is the ejection of atoms from the electrode caused by the bombardment of energetic particles. While useful for processes such as ion etching [6], sputtering would not be favourable for the as the consumption of the electrode material is something to be avoided. Sputtering has the additional downside of potentially contaminating the plasma composition as ejected atoms could end up reacting with the other plasma species.

In a glow discharge there are typically three spatial regions present. These include a *cathode dark space*, a *negative glow* region, and the *anode dark space* [7, 9]. This can be observed in figure 2.4, that shows the potential in each region. Do note, as the distance between the electrodes is increased, additional regions may develop, however these three regions will always persist.

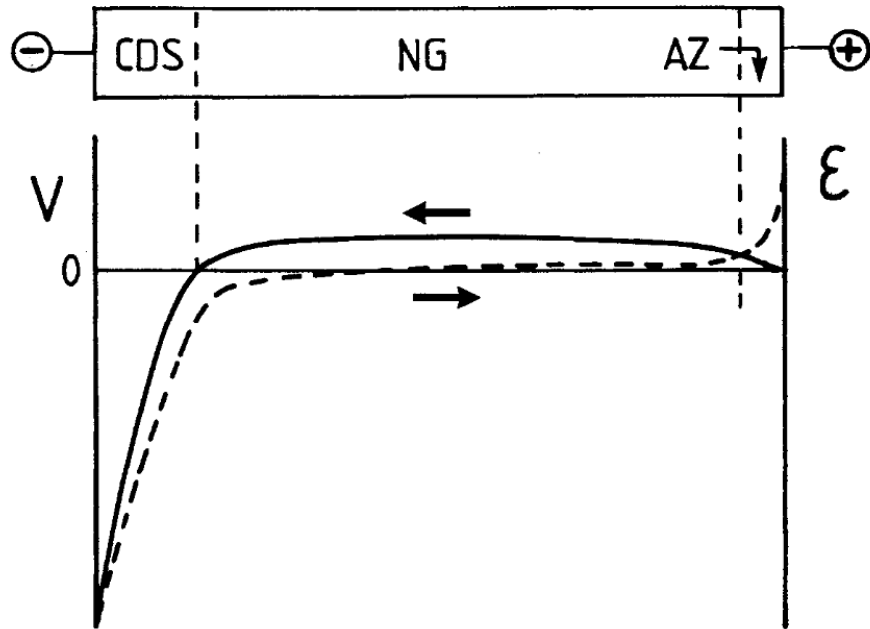


Figure 2.4: Schematic highlighting the regions present in a DC glow discharge [9]. The cathode is on the left and the grounded anode is on the right. (CDS is the cathode dark space, NG is the negative glow, and AZ is the anode dark space.)

The dark space regions are called *sheaths* while the negative glow region is known as the *bulk plasma*. Generally, the sheaths on the cathode will be much larger than that of the anode, as it corresponds to the region where electrons are being accelerated before gaining sufficient energy to cause ionising collisions. In contrast, the anode sheaths form to limit the electron current to the anode, maintaining current continuity over the discharge. Finally, the bulk plasma is the quasi-neutral region that contains the ions and electrons of the plasma.

### 2.2.1 DC Discharge Sources

#### Parallel Plate Designs

The simplest form of a DC plasma source is the *parallel plate design*. As the name suggests, this design involves an anode and a cathode which are separated by a gap in which the plasma is formed. This is the design shown in figure 2.2.

An example of a device using this design can be seen in figure 2.5 of a molecular emission

detector by Eijkel et al[10]. The plasma behaviour of such a design is simply governed by Paschen's law.

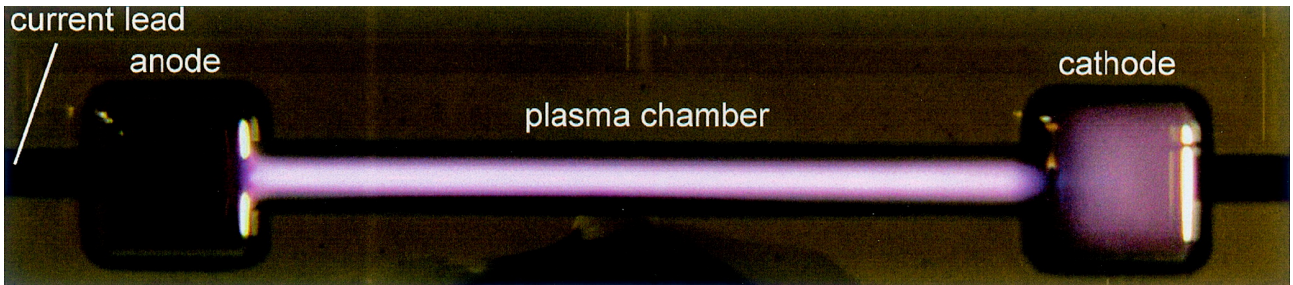


Figure 2.5: A DC plasma from molecular emission detector on chip [10].

Typically, parallel plate designs are favoured when simplicity and low cost are top priorities. There are some use cases such as plasma immersion ion implantation [11] and optical emission detectors [10] where this design proves useful. However in most scenarios, this design is fundamentally flawed due to erosion of the electrode. This erosion is caused by the ion bombardment, which is a necessary process to generate secondary emission electrons; a vital mechanism to sustain the plasma discharge. As such, electrode erosion limits the operating duration of a device with such a design.

### Hollow Cathode Designs

The *hollow cathode design* is a commonly used alternative to the basic parallel plate geometry. Hollow cathodes are typically cylindrical in nature, where the anode remains the same but the cathode has been replaced with cup-like shape that is hollow in the centre (hence the name). An illustration of this can be seen in figure 2.6.

Such a design is favourable over the parallel plate geometry because of a phenomenon known as the *hollow cathode effect*. There are multiple factors that contribute to the hollow cathode effect. However, it is generally agreed upon that the primary mechanism is caused by the pendulum effect of electrons. Electrons, generated via secondary-emissions from the cathode, will tend to oscillate back and forth between the cathode walls. This motion of electrons increases the likelihood that any given one will undergo an ionising collision with a neutral gas atom [13].

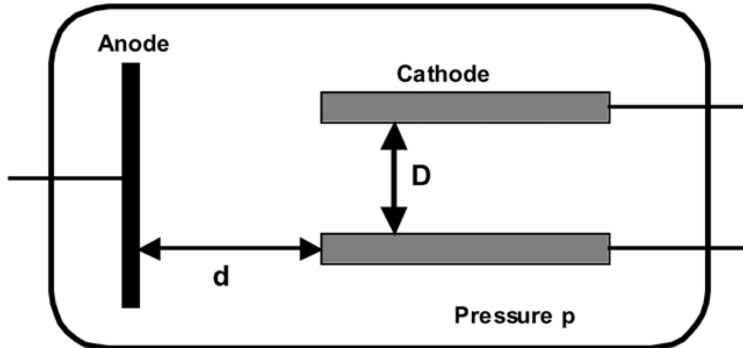


Figure 2.6: A simplified illustration of a hollow cathode design [12].

While the hollow cathode geometry does obey Paschen's law, an additional parameter needs to be taken into account. This new parameter is the diameter of the aperture of the cathode, shown in figure 2.6 as  $D$ . A general rule of thumb is that the product of the pressure and cathode aperture ( $pD$ ) should be in the range of 1-10 Torr cm [14]. When the  $pD$  value is too large, the pendulum effect of the electrons are lost since they do not have sufficient energy to travel to the opposite end of the cathode. In contrast, when the  $pD$  value is too small, the plasma tends to form outside the hollow cathode structure as the diameter of the aperture is comparable to the Debye length [15].

Because of this, hollow cathodes have several benefits compared to their parallel plate counterparts. The most notable is that they have a lower breakdown voltage, particularly at lower gas pressures [16, 17]. Additionally, they generally produce a higher current density for a given operating voltage [16, 18], as illustrated in figure 2.7.

However, there are still several drawbacks to the hollow cathode. For one, the pendulum effect of electrons also applies to the ions, which means greater bombardment of the cathode, thus leading to faster erosion. The ion bombardment also as the side effect of causing increased heating of the cathode, resulting in thermionic emission. While this increases the electron emission, this also further contributes to the cathode erosion.

Despite this, advancements and developments of the hollow cathode geometry have mitigated this by extending the life and reliability of the cathode. As such, hollow cathode designs are found in research areas such as electron beam guns [19, 20] for welding and 3D printing of

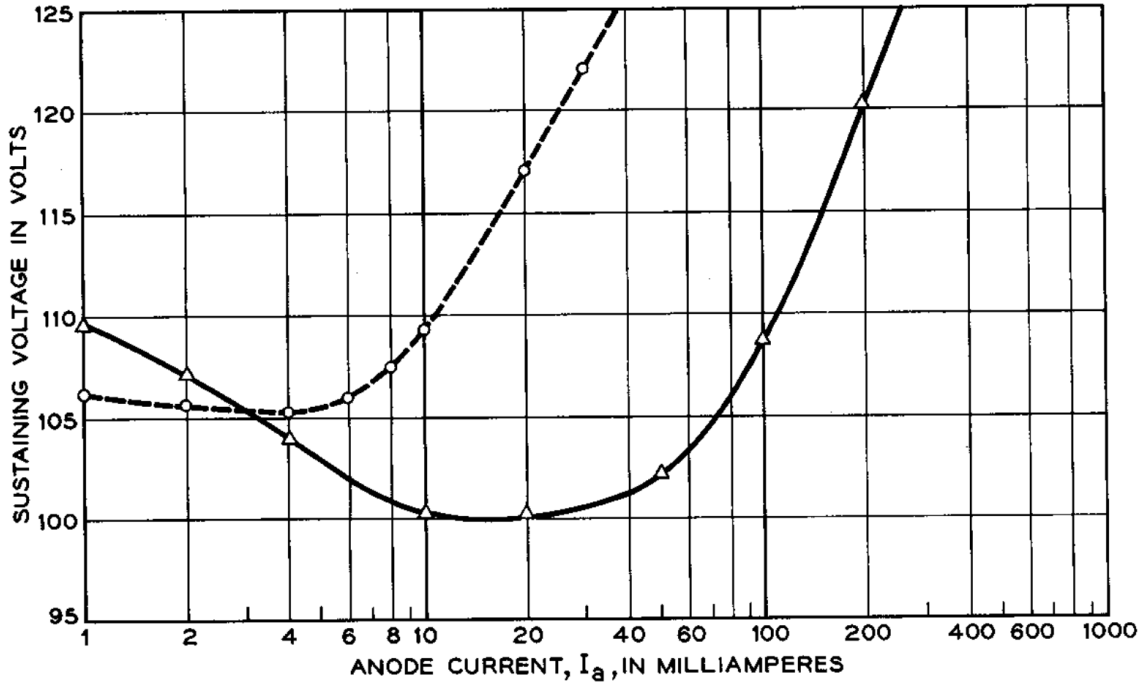


Figure 2.7: A comparison of the voltage vs current curve for a hollow cathode geometry (solid line) and a typical parallel plate geometry (dashed line)[14].

metals, and electrostatic propulsion [21] for spacecraft thrusters.

## 2.3 AC Discharge

If the voltage source in the circuit of figure 2.2 were to be replaced with a low frequency AC source, the discharge behaviour would be almost identical to that of the DC discharge, with the caveat that the roles of the electrodes alternating between cathode and anode. This is provided that the half time period of an AC cycle is larger than the duration for ions and electrons to move across the electrodes [9].

However, as the frequency of the AC source is increased, typically to the region of radio or microwave frequencies, there is an asymmetry between the movement of the ions and electrons. The electrons are capable of responding to the change in the electric fields relatively quickly; however, due to the ions being significantly heavier than electrons, they have a much slower response time that is restricted by their inertia [22].

Since the ions cannot respond to the changing electric field quick enough, they respond to the time-averaged field thus are accelerated against both electrodes cross the sheath. On the other hand, the electrons begin accelerating through the bulk plasma towards the anode during the first half period of the AC signal. Then as the direction of the electric field reverses in the second half period of the signal, the positions of the anode and cathode flip, and any electron that has not collided with the original anode (which is now the cathode), gets accelerated through the bulk plasma towards the new anode. This oscillating behaviour confines the electrons, resulting in an increased likelihood of ionising collisions with the neutral background gas. This mechanism is similar to the pendulum effect of the electrons in hollow cathode DC discharges. As the frequency of the AC source is increased, more electrons become trapped in this regime, hence it is no surprise that the breakdown voltage of the plasma decreases [23]. This can be seen in figure 2.8

Astute readers may notice the minimal role of the secondary emission of electrons plays in the AC discharge. Because of the reduced of ion bombardments, there is less erosion on the electrodes, which increases its overall lifetime.

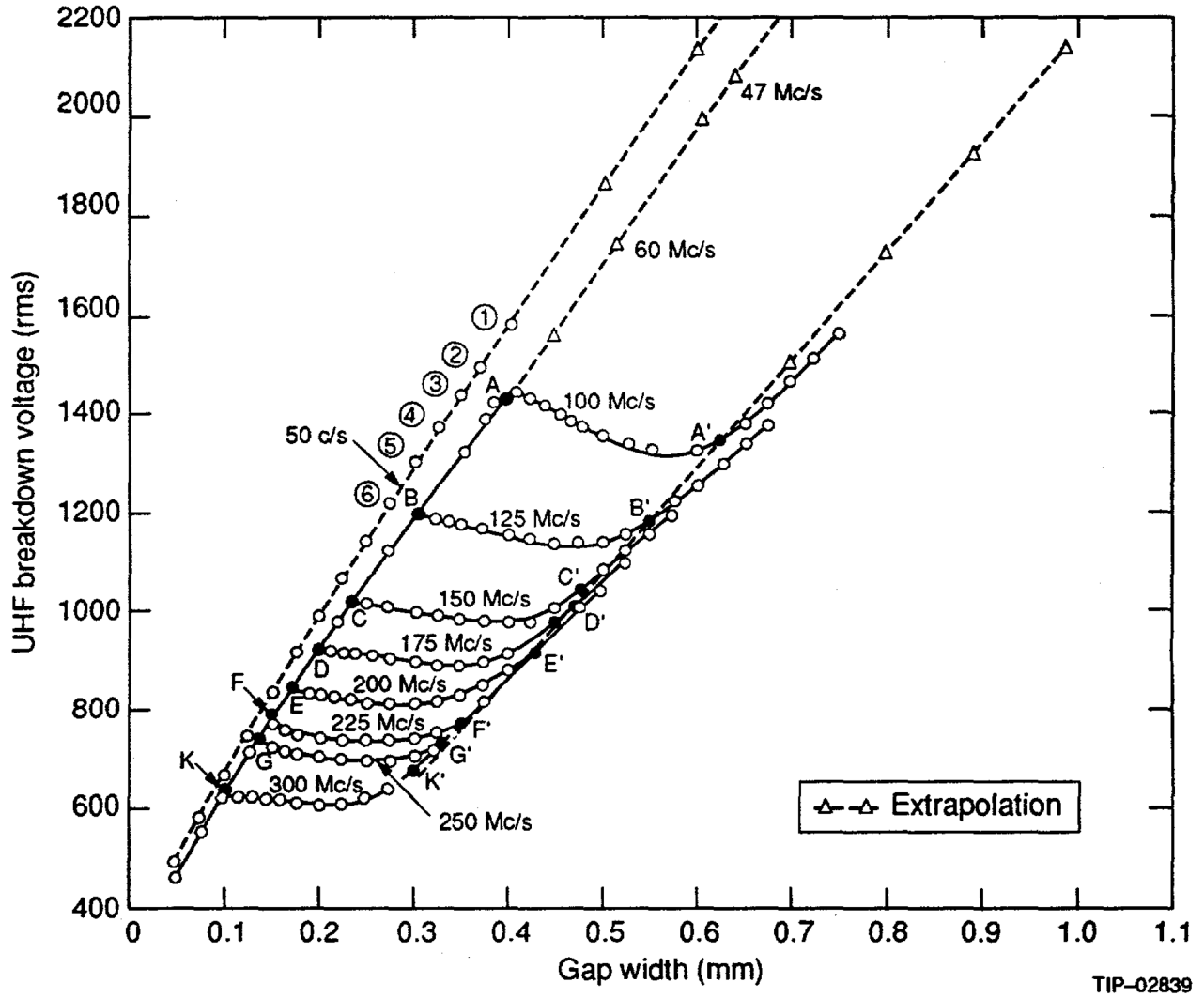


Figure 2.8: Paschen curve for AC discharge across various frequencies [24].

### 2.3.1 AC Discharge Sources

#### Capacitively Coupled Plasma Designs

*Capacitively coupled plasma* (CCP) reactors are one of the simpler designs for AC discharges. The design is very similar to the parallel plate geometry seen in figure 2.2, however rather than a DC power supply, one or more radio frequency (RF) sources are used. Additionally, a capacitor can be added to eliminate and DC bias introduced by the source or matching networks. An example of a CCP design can be seen in figure 2.9. These reactors typically operate at the approved ISM frequency of 13.56 MHz, however frequencies up to 100 MHz have been used as demonstrated by Sharma et al [25].

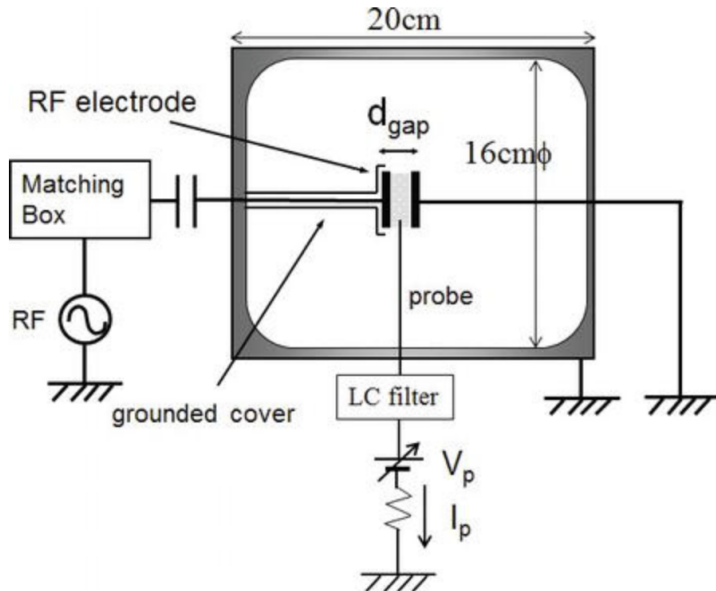


Figure 2.9: Illustration of a capacitively coupled plasma (CCP) experimental setup [26].

CCP sources are primarily used in the semiconductor industry for thin film deposition and etching. This is due to the simple design which can be scaled fairly inexpensively. Another benefit of CCPs is that the electron temperature is fairly uniform across the entire reactor, as seen in figure 2.10.

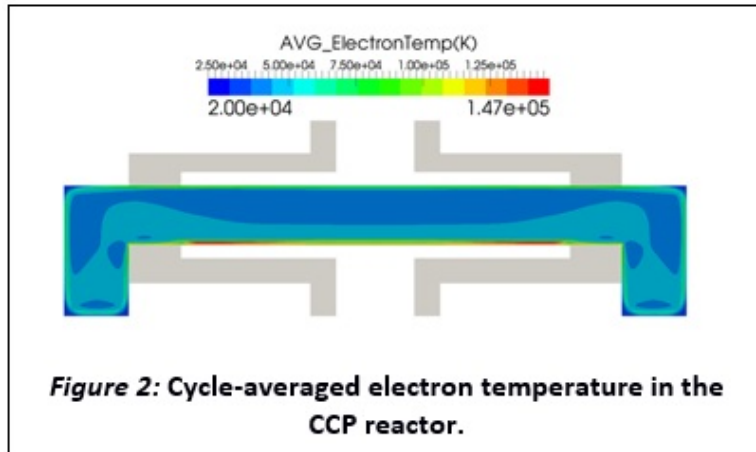


Figure 2.10: Cycle averaged electron temperature in a CCP reactor [27].

However, the biggest drawbacks with CCP designs has to do with the limited plasma density, typically on the order of  $10^9$  to  $10^{10}$   $\text{cm}^{-3}$  [28? ]. Simply increasing the input power does not translate to an increased plasma density due to energy loss by ions [15]. Increasing the frequency can help with reducing the breakdown voltage and increasing density, however this is discussed later in this chapter.

Solutions for this include dual frequency driven CCPs such as the ones by Lee and Hong [29]. The idea behind such a design is that the higher frequency source controls the plasma density while the lower frequency source controls the energy of the ions. Other solutions including adding magnets and incorporating a hollow cathode shaped electrode to CCPs to confine the energetic electrons near the electrode [26].

### Inductively Coupled Plasma Designs

Another type of AC discharge source is the *inductively coupled plasma* (ICP) design. Unlike other reactor designs, ICPs do not have electrodes. Rather it relies on the electric current generated by electromagnetic induction. This changing magnetic field is typically achieved with the use of a solenoid; an example of this is seen in figure 2.11.

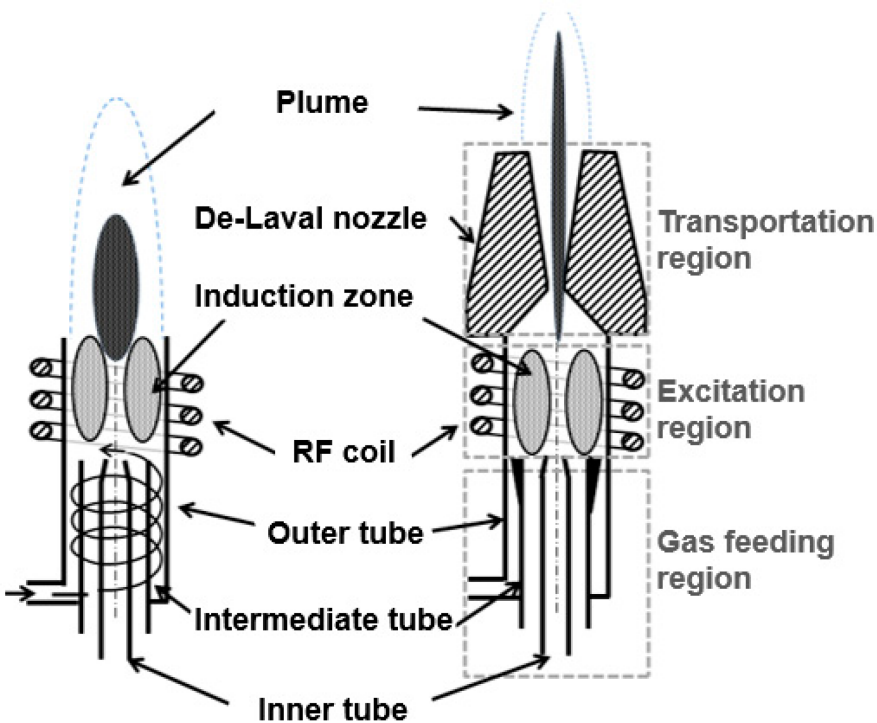


Figure 2.11: Schematic of inductively coupled plasma (ICP) torches [30].

Because of the lack of electrodes, ICP reactors do not experience electrode erosion from ion bombardment or contamination of feed gas from sputtering. Another advantage of the ICP design is that when compared to CCPs, they tend to generate a higher plasma density, especially at lower pressures. A comparison of ICP and CCP properties was done by Sakamoto et al

[31], seen in figure 2.12. The results show that the electron density of ICPs were an order of magnitude greater than that of CCPs, though this did come with a drop in electron temperature.

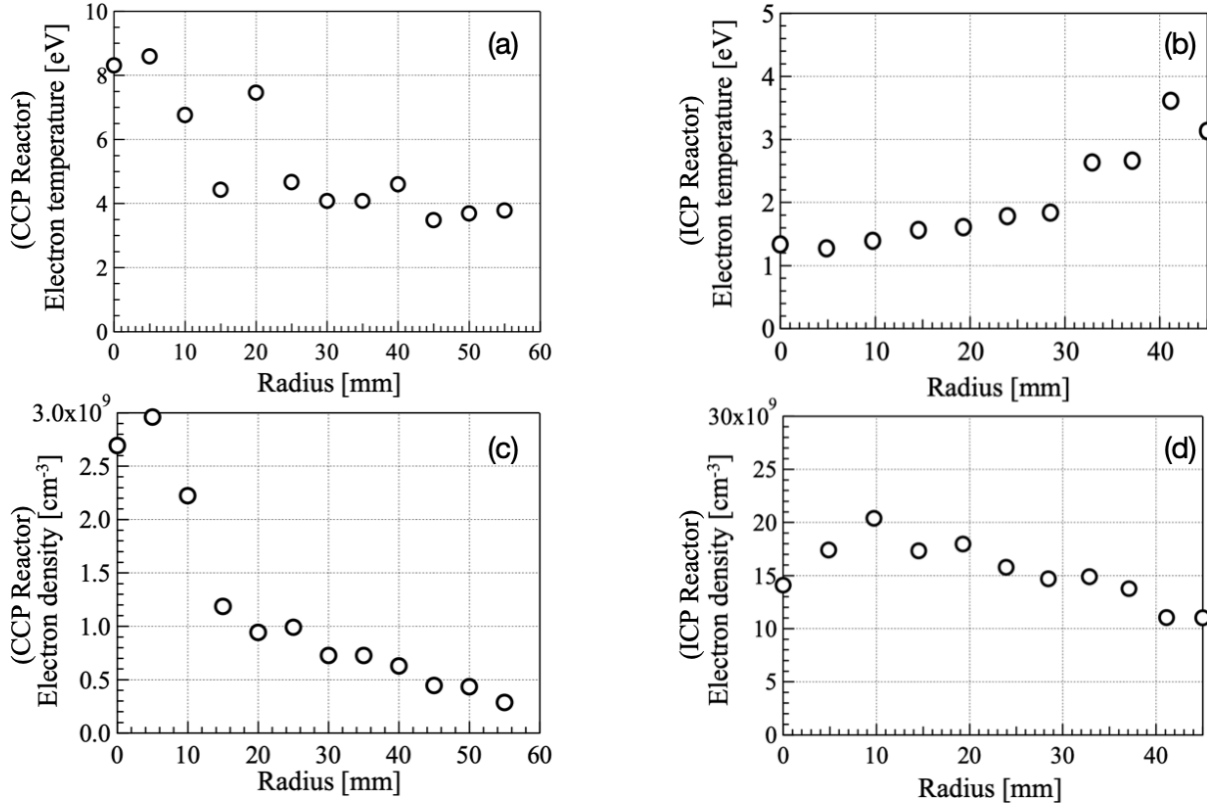


Figure 2.12: Comparison of plasma parameters between CCP and ICP reactor [31]. The two left most graphs (a, c) are the results from a CCP reactor, while the two right most graphs (b, d) are the results of the ICP reactor. The top two graphs (a, b) show the radial distribution of electron temperatures for a CCP and ICP reactor respectively. The bottom two graphs (c, d) show the distribution of electron density for a CCP and ICP reactor respectively.

However, it has been observed that this advantage of plasma density does not necessarily continue as the size of ICPs are miniaturised. This is because the rate of decrease of inductance in the coil is much higher when compared to the parasitic resistance [15]. Another downside is that ICPs are only viable at lower pressures. This is because the current in the coil required to sustain the plasma is quite high at atmospheric pressures, thus pressures between 0.1–10 Torr are typically used [32].

Much like CCP reactors, ICP reactors are also used in the semiconductor industry, however they each serve different functions. For example, ICPs are used for etching of conductors whereas CCPs are used for the etching of dielectrics [33]. Another example of ICP sources are in ICP

mass spectrometry, where they produce better precision compared to other techniques.

## Dielectric Barrier Discharge Designs

*Dielectric barrier discharge* (DBD), sometimes referred to as silent discharge, is a fairly common design used on a large industrial scale. A typical DBD design can be seen in figure 2.13. Much like the parallel plate discharge, there are two electrodes, however DBD designs require the presence of at least one dielectric material in the discharge gap.

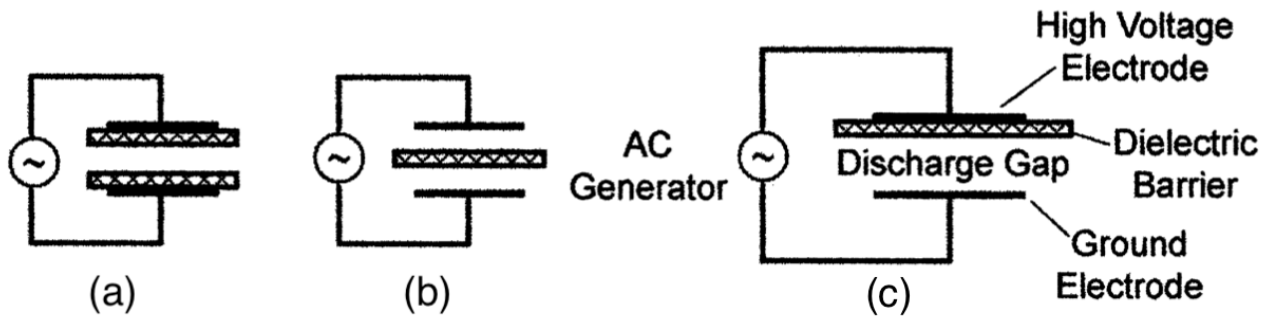


Figure 2.13: Examples of different Dielectric Barrier Discharge (DBD) designs [34]. The left most (a) and right most (c) drawings show at least one dielectric on the electrodes, while the middle (b) illustrates a dielectric in the discharge gap, but not touching the electrodes.

Due to the dielectric being an insulator, no conduction current can flow between the electrodes, strictly limiting DBDs to AC operation. This layer of dielectric performs two functions. The first is that it protects the electrodes from ion bombardments, preventing erosion. Secondarily, the dielectric plays a role in limiting the average current density of the discharge, thus behaving as a ballast to prevent the transition of glow discharge to arc discharge [34].

Most DBD devices operate in the kHz frequency range but experiments have been performed for reactors up to approximately the 10 MHz range [35]. This is because the dielectric constant of the substrate decreases at high frequencies, making it less effective at limiting the current [34].

DBD designs were frequently used in plasma display panels, which were fairly ubiquitous in televisions until about a decade ago. Nonetheless, DBD reactors still have applications ranging from surface treatment of materials to the gas treatment such as generation of ozone from air

[36].

### Microwave Discharge Designs

All previous examples of AC discharges discussed so far have operated in the RF region of the electromagnetic (EM) spectrum. While there are various standard for radio bands set by agencies such as the International Telecommunication Union (ITU) or the Institute of Electrical and Electronics Engineers (IEEE), it is convention to class frequencies above 300 MHz as microwave.

The microwave plasma sources commonly used in industry tend to be fairly large devices. One of the most common of these devices generate the plasma via *surface wave discharge* where the microwaves are propagated by a wave guide [37]. Yet another type of microwave source is the *electron cyclotron resonance* plasma reactor, which utilise magnets to induce an acceleration of the electrons via the Lorentz force, thus enabling it to achieve high plasma densities [37]. An illustration of both these methods can be seen in figure 2.14 and 2.15 respectively.

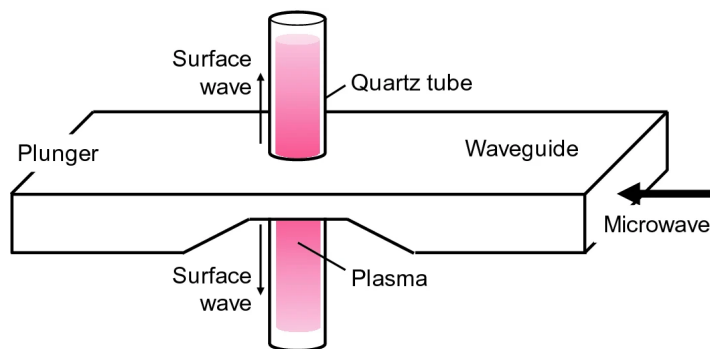


Figure 2.14: Schematic of a surface wave discharge plasma source [37].

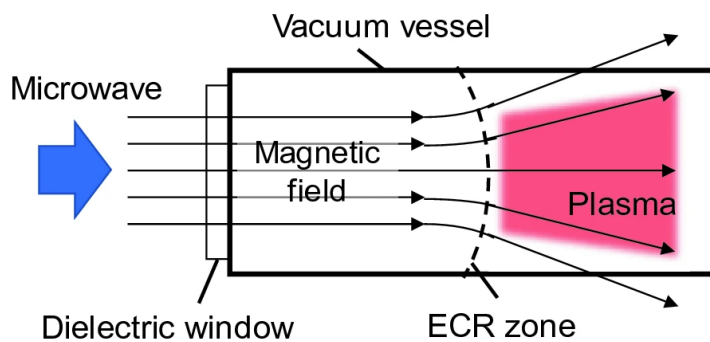


Figure 2.15: Schematic of an electron cyclotron resonance plasma source [37].

While these larger microwave plasma reactors are very efficient, their size and costs make it unsuitable for testing in a laboratory setting. Miniaturising such designs are also unfeasible as the size of the device determines the frequency of operation; for example a source that is approximately 1 cm would require a power supply capable of operating at around 30 GHz.

However, smaller plasma sources have been developed that utilise stripline technologies that are capable of generating using RF and microwave frequencies [38, 39]. Examples of these microstrip plasma sources can be seen in figure 2.16.

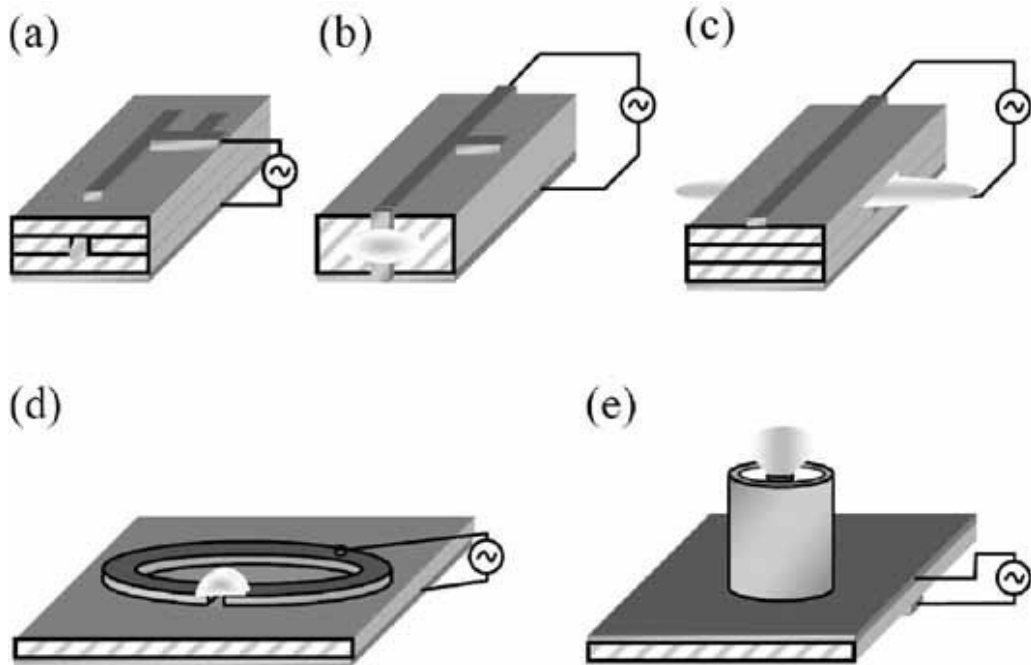


Figure 2.16: Examples of different types of microstrip plasma sources [15]. The top three designs (a, b, c) are linear microstrip resonators, while (d) shows a microstrip split-ring resonator, and (e) illustrates a coaxial resonator.

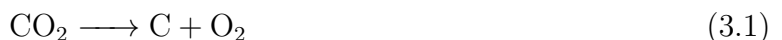
Since dimensions of the plasma formed by these microstrip sources are much smaller compared to the excitation wavelength, they can essentially be modelled as a CCP source. But since the microstrip sources operate at microwave frequencies, it is able to take advantage of the efficiency gains obtained by using higher frequencies as shown in figure 2.8, and has also been shown to increase the plasma density [40].

# Chapter 3

## Carbon Dioxide Splitting

### 3.1 Traditional Process

Before understanding the process of plasma-assisted CO<sub>2</sub> splitting, it would be useful to briefly explain the traditional thermally driven process. This process, sometimes referred to as pure CO<sub>2</sub> splitting, can take one of two possible forms. Often referred to as the reverse of coal burning, the overall reaction for CO<sub>2</sub> splitting can be written as:



This though is a simplification of the process, as it is most likely a two part mechanism [41]. The first half of the process would involve splitting the CO<sub>2</sub> into carbon monoxide (CO) and atomic oxygen (O) as seen in 3.2. The second step could take one of two possible pathways, however the most likely of the two would be the Boudouard reaction, seen in 3.3; however, this specific reaction is beyond the scope of this report.



Traditional thermal CO<sub>2</sub> splitting has not had much success to date, primarily due to the fact that CO<sub>2</sub> is an incredibly stable molecule with a Gibbs free energy of formation ( $\Delta G^\circ$ ) of -394 kJ mol<sup>-1</sup>. This is significantly higher than most other common gases as illustrated in figure 3.1.

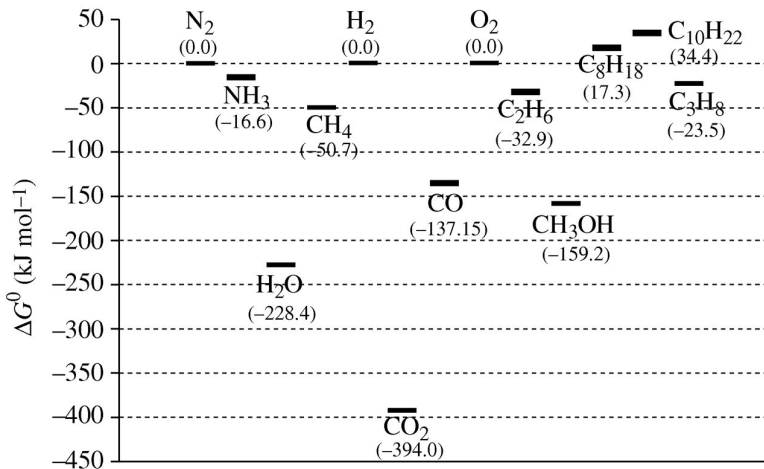


Figure 3.1: Gibbs free energy of formation for different chemicals based on data from the NIST database. [42]

The enthalpy of formation ( $\Delta H_f^\circ$ ) of the reaction in 3.2 is +283 kJ mol<sup>-1</sup>, meaning that it is endothermic. Thus in order to make this reaction favourable, high temperatures are required. Figure 3.2 highlights the conversion of such a reaction based on temperature, along with its corresponding energy efficiency [43]. This process could be improved by the presence of an active catalysts but this also increase the complexity and costs.

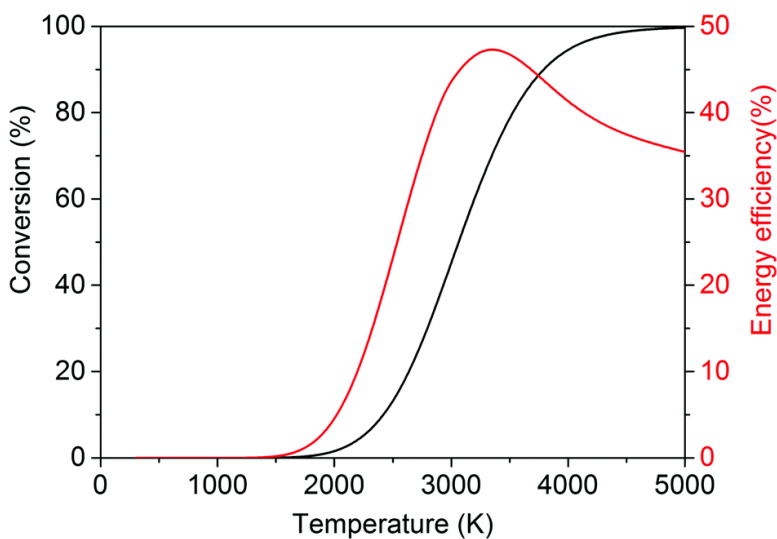


Figure 3.2: Thermal conversion and energy efficiency of CO<sub>2</sub> splitting as a function of temperature. [43]

Because of the low energy efficiency of pure CO<sub>2</sub> splitting, it is oftentimes more practical to include the use of a co-reactant. Ideally, this is done using a co-reactant with a higher Gibbs free energy (i.e. a less negative value) [42]. In the literature, the most common co-reactants for CO<sub>2</sub> splitting are methane (CH<sub>4</sub>, ΔG° = -50.7 kJ mol<sup>-1</sup>) and hydrogen (H<sub>2</sub>, ΔG° = 0.0 kJ mol<sup>-1</sup>).

The CO<sub>2</sub> splitting with CH<sub>4</sub> is a reaction that generates synthesis gas (syngas), principally used in the production of ammonia and methanol []. The process is referred as the dry reforming of methane and can be expressed as:



This reaction is also endothermic, with a ΔH<sub>f</sub>° = +247 kJ mol<sup>-1</sup>, hence has to be run at high temperatures (between 1000 K to 1300 K, much lower than that of pure CO<sub>2</sub> splitting) and in the presence of a catalysts (typically nickel) [44]. However, the big limitation with this process is the formation of soot on the catalyst, reducing the yields.

As for using H<sub>2</sub> as a co-reactant to CO<sub>2</sub> splitting, this process is known as the Sabatier reaction. The reaction, seen in 3.5, is typically to generate synthetic natural gas but has other uses such as the production of water on the international space station [45].



The reaction is exothermic, with a ΔH<sub>f</sub>° = -165.3 kJ mol<sup>-1</sup>, but does require a catalyst in order to achieve high conversion yields. Nonetheless, there are two issues with this process. The first being, unless water is the desired end product, a third of the H<sub>2</sub> used goes towards the creation of a waste product; not ideal when using this process at scale. The other issues has to do with the fact that most of the world's supply of H<sub>2</sub> comes from the process of steam reforming, which produces CO<sub>2</sub> as a by-product.

## 3.2 Plasma-assisted $CO_2$ Splitting

As highlighted above, there are several shortfalls with the traditional process of  $CO_2$  splitting. This is where the use of plasma, specifically non-thermal plasmas (i.e. generated by electric means), can be beneficial. In these plasmas, electrons have a higher temperature than the ions or the background gas. Energetic electrons in the plasma can dissociate molecules, even highly stable ones such as  $CO_2$  at standard temperatures and pressures [43].

Because of this behaviour, there is no need for heat and pressurised reactors, reducing the complexity (and thereby costs). This leads on to the second benefit, where the entire operation of such a reaction is described as a 'turn-key' process due to the ability to instantly turn the plasma on and off, with minimal stabilisation times. There is also no need for rare earth metals to be used as catalysts, and it has been shown that plasma reactors can have good scalability as shown by Kogelschatz in [46].

There are several different methods to generate plasma for  $CO_2$  splitting in the literature, however the most common are: dielectric barrier discharges, gilding arc discharges, and radio frequency(RF)/microwave discharges. This report will only cover the RF/microwave discharges as it is the process being used, with several examples in the literature highlighted below.

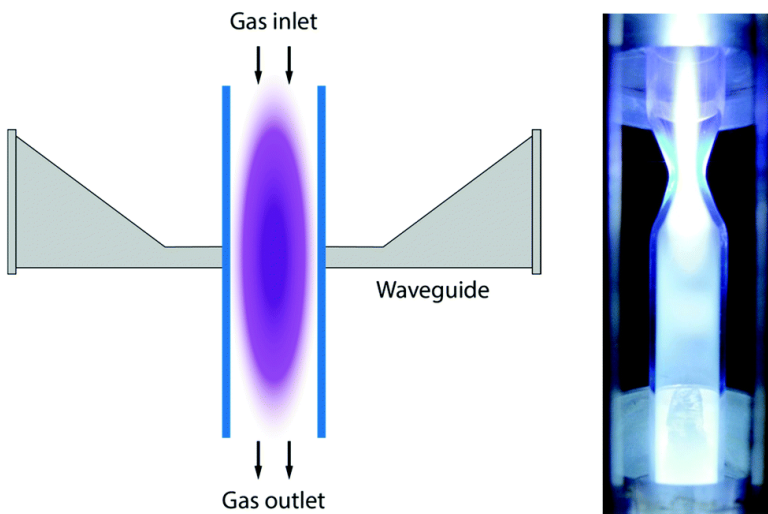


Figure 3.3: Schematic of microwave reactors for  $CO_2$  splitting. [43]

Many experiments utilise a structure as seen in figure 3.3, whereby the gas is fed in via a quartz tube coupled with an external wave guide where the microwave discharge is generated. Such

a design was used by Spencer and Gallimore [47] to achieve a conversion efficiency of approximately 90%; although this came at the cost of energy efficiency which reached a maximum of 3%. The authors went on to state that such a system would not be suitable for CO<sub>2</sub> emission reductions.

Nonetheless, other designs for RF/microwave discharges exist such as the one developed by Xu et al [48]. Their design utilised a co-reactant called *trans*-stilbene. Unlike the co-reactants previously mentioned, which were gaseous, *trans*-stilbene is a liquid. Because of this, the plasma had to directly contact the solution, which was achieved via a plasma jet reactor. The jet nozzle had to be placed 4 mm above the surface of the liquid, and the final product of this reaction was CO and epoxides (a popular compound use for detergents, adhesives, and plastics). The authors were able to obtain a 75% yield on epoxides and a splitting of approximately 70% of the CO<sub>2</sub> in the plasma. As such, this will be the process that is emulated in this report.

# Chapter 4

## Split Ring Resonator

In the work done by Xu et al [48], the plasma discharge was generated using a CCP jet, specifically a design by the European Cooperation in Science and Technology (COST) [49]. The COST plasma jet was originally developed for medical and biomedical applications, as such were developed to operate at the approved ISM frequency of 13.56 MHz. However, RF plasma sources are flawed in the sense that they have a limited plasma density, which could theoretically limit the rate of splitting of CO<sub>2</sub> molecules.

To mitigate this, this project attempts to emulate the process of CO<sub>2</sub> splitting using a microwave plasma, specifically a microstrip-based source called the *split ring resonator* (SRR). Using such a device will have three benefits. First, the power efficiency of the microwave plasmas would allow for discharges to occur on the order of milliwatts (mWs) rather than watts (W). The device would also be much smaller and cheaper to manufacture. Finally, as mentioned in section 2.3.1, operating at a higher frequency should increase the plasma density.

An illustration of an SRR can be seen in figure 4.1. The design of a SRR is quite simple, consisting of a conducting ring, usually made of copper, laid on top of a dielectric substrate. The bottom of the dielectric consist of a ground plane that covers the entirety of the surface. This has the added benefit of dispersing the heat generated from the SRR. As seen in figure 4.1, there is a small gap made on the top surface that breaks the copper ring, which is where the plasma discharge occurs.

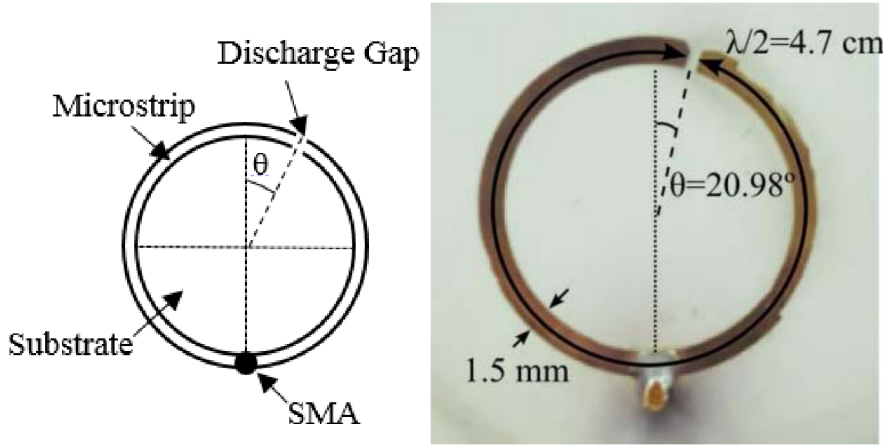


Figure 4.1: Schematic (left) and photo (right) of SRR [50].

## 4.1 Overview

In order to achieve a discharge, a high frequency (microwave) voltage is applied to the SRR via the SMA connector. The exact frequency to be used is governed by two factors: the mean circumference (which is measured from the middle) of the top conducting ring and the dielectric constant of the substrate used. The mean circumference is specifically designed to be half the wavelength corresponding to the desired frequency. The dielectric constant is required to determine the speed of light in the dielectric medium used. Thus, an equation for the frequency used for a given SRR is [50]:

$$f = \frac{c}{\lambda\sqrt{\epsilon_r}} \quad (4.1)$$

The reason why the mean circumference is designed to be half the desired wavelength is for power efficiency. Due to this design, the ends of the SRR (i.e. where the gap is) will be  $180^\circ$  out of phase from each other. Because of this, when one end of the SRR is at the peak of the AC cycle, the other will be at a trough; thus the potential difference between the two ends has been doubled. This geometric trick allows for the doubling of the strength of the electric field at a constant power.

Astute readers may notice another peculiarity with the SRR seen in figure 4.1, in that it is not symmetrical. Instead, the discharge gap appears to be offset towards one side of the device.

This is deliberate as the offset gap allows for the impedance matching of the SRR to the impedance of the power supply used, thus maximising the power transfer. This offset angle is measured from the very centre of the ring, and is determined using the expression [51]:

$$\theta = \arccos\left(1 - \frac{Z_{in}\pi}{Z_0 Q}\right) \quad (4.2)$$

where  $Z_{in}$  is the input impedance of the power supply,  $Q$  is the quality factor, and  $Z_0$  is the characteristic impedance of the SRR. Typically, the input impedance of many power supplies is  $50 \Omega$ . The characteristic impedance is governed by four factors: the width of the top copper trace, the thickness of the copper pour, the thickness of the dielectric substrate, and the dielectric constant of the substrate. Wheeler derived an analytical solution, see equations 4.3-4.6, that approximates the characteristic impedance with an error of less than 1% [52]. As for the quality factor, this parameter is given on the data sheet of the substrate used.

$$Z_0 = \frac{42.4}{\sqrt{1 + \varepsilon_r}} \left[ 1 + \frac{4h}{w'} (X_1 + X_2) \right] \quad (4.3)$$

$$X_1 = \frac{4h}{w'} \left( \frac{14\varepsilon_r + 8}{11\varepsilon_r} \right) \quad (4.4)$$

$$X_2 = \sqrt{\left(\frac{4h}{w'}\right)^2 \left(\frac{14\varepsilon_r + 8}{11\varepsilon_r}\right)^2 + \pi^2 \frac{1 + \frac{1}{\varepsilon_r}}{2}} \quad (4.5)$$

$$w' = w + \frac{t}{\pi} \ln \left[ \frac{4e}{\sqrt{\left(\frac{t}{h}\right)^2 + \left(\frac{t}{w\varepsilon_r + 1.1\pi}\right)^2}} \right] \frac{\varepsilon_r + 1}{2\varepsilon_r} \quad (4.6)$$

where  $w$  is the width of the top copper trace,  $t$  is the thickness of the copper pour (typically specified by the PCB manufacturer), and  $h$  is the height of the dielectric substrate.

## 4.2 Production

The SRR device used in this project introduces a slight modification to the design of the traditional SRR. In order to create a small jet of plasma, through holes are needed at the region of the gap of the SRR. This would allow the gases to react with the plasma, then pass through the hole.

However, to determine if this small change had any significant effects on the behaviour of the SRR, simulations were run to better understand the discharge dynamics. Specifically, *Particle-in-cell* (PIC) simulations were used; and the software used is called *XOOPIC* [53]. Further information on PIC simulations and XOOPIC can be found in the appendices.

### 4.2.1 Simulations

Multiple different simulations were run to understand the characteristics of the plasma, however they could be broadly broken down into three groups. For all these simulations, a cross sectional plane of the discharge gap of the SRR was modelled. The reasoning for this was that the plasma formed would typically be constrained around the gap [? ]. Though the ring of the SRR is a circle, the discharge gap is small relative to the overall device, hence can be approximated to be a rectangle. For all the following simulations, the parameters can be found in table 4.1 unless specified otherwise.

Table 4.1: Simulation parameters of SRR in XOOPIC.

Parameters	Value	Units
Domain x-axis	1.0	mm
Domain y-axis	2.5	mm
Dielectric thickness	500	$\mu\text{m}$
Dielectric constant	3.66	
Equipotential thickness	40	$\mu\text{m}$
Gas pressure	780	Torr
Gas temperature	25	meV
Potential Difference	150	V
Frequency	1	GHz
Time step	0.1	ps

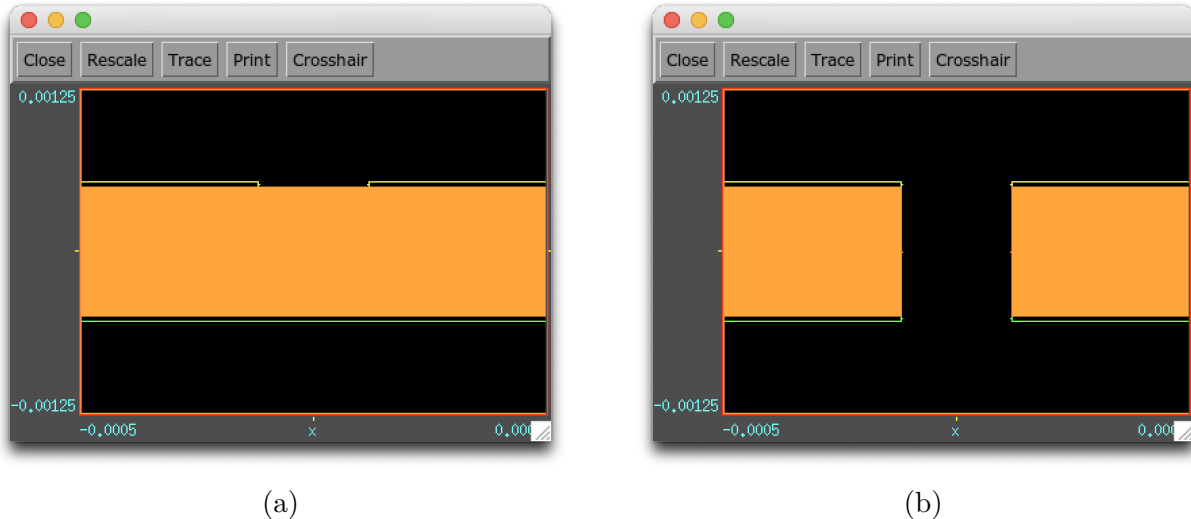


Figure 4.2: A cross section comparison of SRR simulation domain without a hole (a) and with hole (b) in gap.

The first of these simulation groups was to simply study the effects of introducing a through hole to the SRR. For this test, all simulation parameters were kept identical, the only difference would be the introduction design of the gap. A visualisation of the simulation domain is shown in figure 4.2. In figure 4.2a, the dielectric substrate (seen in gold) and the bottom electrode (seen in green) is kept intact as a single structure, whereas the top electrode (seen in yellow) is split. However in 4.2b, all three layers of the SRR are split into two. The size of the discharge gap chosen was  $240 \mu\text{m}$ . In both cases, the dielectric constant of the substrate was 3.66, and the voltage used was 150 V at 1 GHz.

The results of the simulation after it stabilised can be seen in figure 4.3. The immediate difference that can be observed is the fact that the ions and electrons, represented as blue and orange dots respectively, tended to ‘sit’ deeper into the gap in the case with the through hole. Intuitively, this would make sense as these particles are not colliding with the substrate (which in XOPIC meant that they were removed from the simulation domain). Additionally, it was hypothesised that strength of the electric field between the top electrodes and the ground plane could potentially play an effect in how deep the ions and electrons penetrate in the gap of the SRR and control the average electron energy.

This leads into the second group of simulations that were run, where the separation distance between the top and bottom electrodes were investigated, which also had the added benefit of

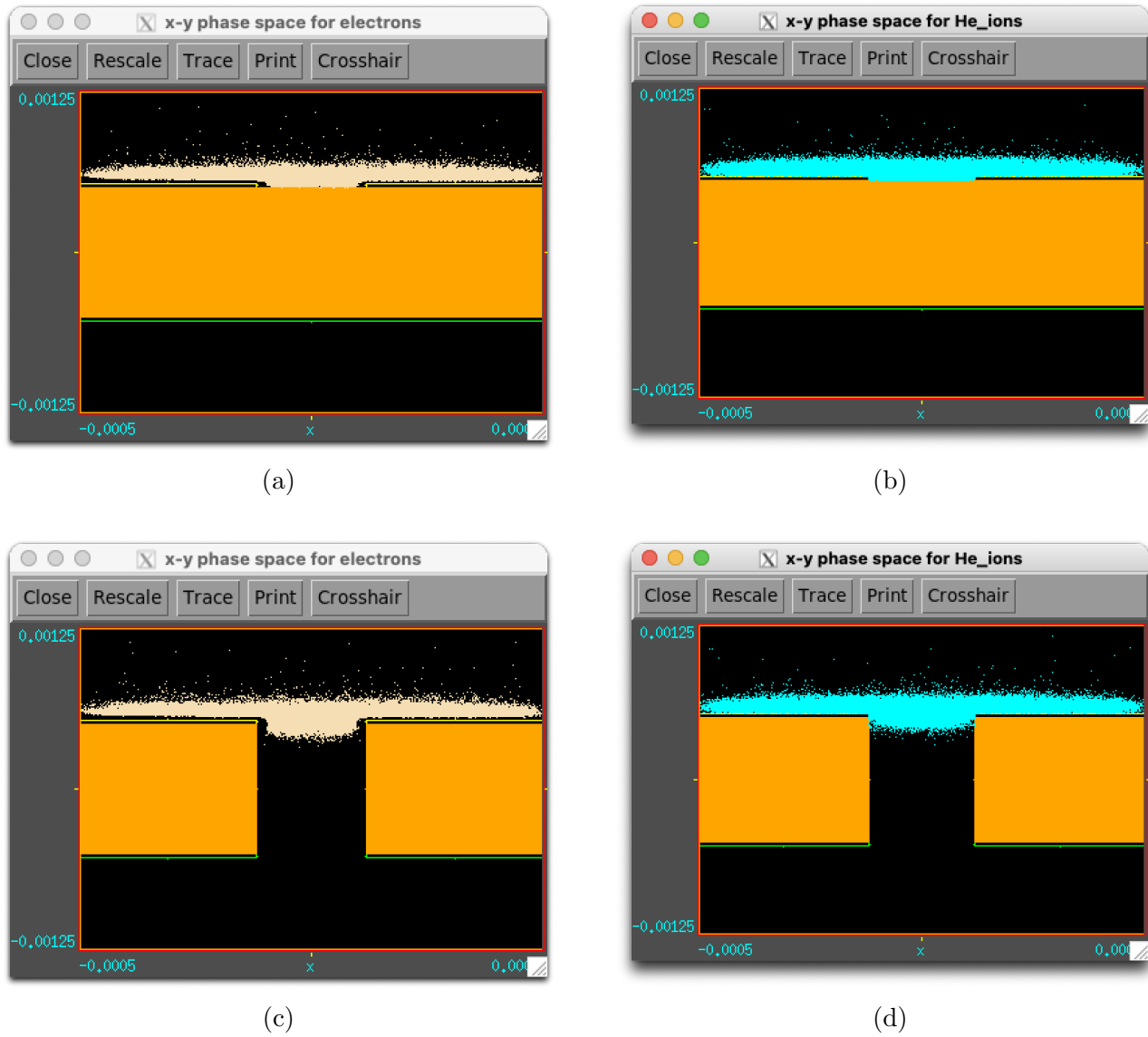


Figure 4.3: A comparison of the distribution of electron (a, c) and ions (b, d) in the discharge of the SRR. The top two subfigures (a, b) show the distribution in an SRR with no hole, while the bottom two (c, d) show the distribution in an SRR with a hole in the gap.  
Comparison of SRR with and without hole in gap.

identifying the ideal dielectric substrate thickness to be used when manufacturing the SRR. The parameters used for the size of the gap, the dielectric constant of the substrate, and the potential difference were kept the same as the first group. As for the dielectric thickness, simulations were run with values of 0.2 mm, 0.5 mm, 1.0 mm, 1.5 mm, and 2.0 mm.

From the cross sectional view of the density plot of electrons in figure 4.5, all simulations performed quite similarly. The electrons seem to extend through the gap by roughly the same distance. However, even though the dielectric thickness did not play a large role in the plasma, it would be preferable to choose a thicker dielectric for the sturdiness of the board.

The final group of simulations run were to establish the effect of the discharge gap widths. The sizes used were a gap width of 120  $\mu\text{m}$ , 240  $\mu\text{m}$ , 360  $\mu\text{m}$ , and 480  $\mu\text{m}$ .

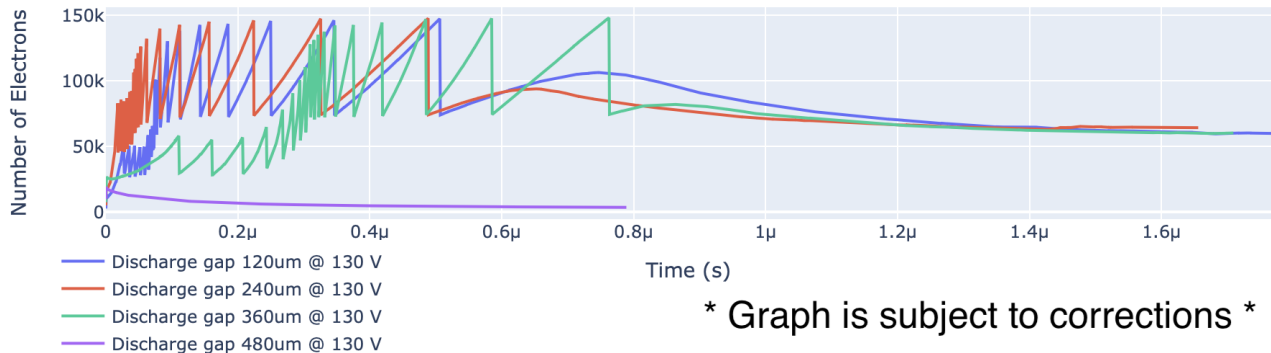


Figure 4.4: Time series plot of number of electrons across different discharge gaps.

The results of these simulations can be seen in figure 4.4. From these tests, only three simulations were successful as the run with a gap width of 480  $\mu\text{m}$  lost all the electrons. The reasons for this behaviour was that the voltage used (150 V) was not sufficient to ignite a discharge, as the electric field in the gap reduces with an increase in gap width. As for the other three runs, the big difference seemed to be the initial growth rate. A gap width of 240  $\mu\text{m}$  appeared to be the optimum. One would expect that the smallest gap width would perform the best, however as seen by Paschen's law (refer to Chapter 2.1), reducing the distance between electrodes too much would cause the electrons to be simply lost to the electrode. This could possibly explain why the run with a 120  $\mu\text{m}$  gap performed worse than the run with a gap width of 240  $\mu\text{m}$ .

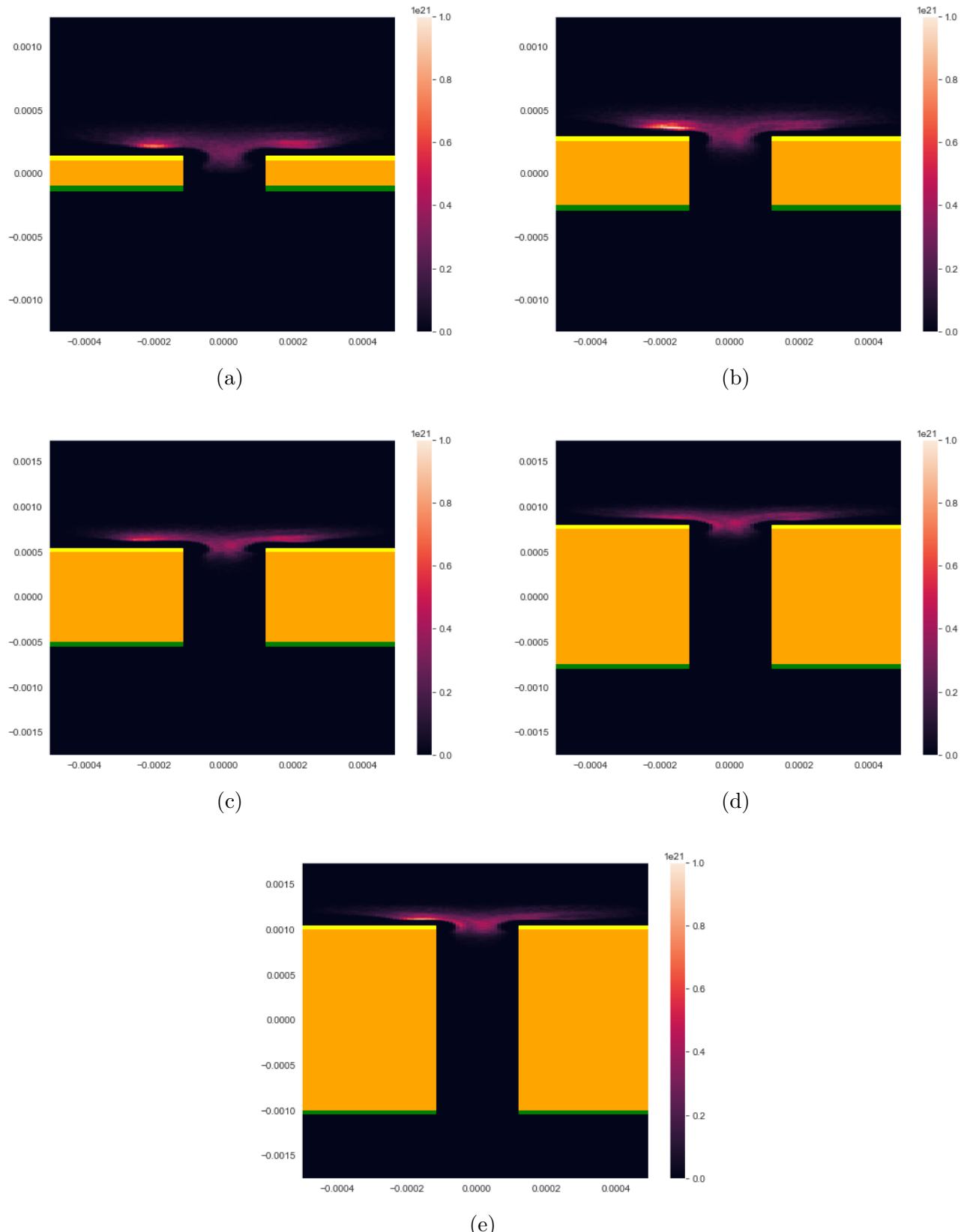


Figure 4.5: Comparison of dielectric thickness of 0.2 mm (a), 0.5 mm (b), 1.0 mm (c), 1.5 mm (d), and 2.0 mm (e) on the SRR.

### 4.2.2 Design

Armed with this information, a design of the SRR to be used was made. The first step was to select the PCB substrate to be used, as its dielectric constant is a central parameter for all other calculations of the SRR. The material selected was the RO4350B<sup>TM</sup> material from Rogers corporation. This specific material was chosen as it is designed for high power UHF designs, and its relatively low fabrication costs. Additionally, the RO4350B<sup>TM</sup> material did not require any special treatments or procedures to introduce a through hole. According to its data sheet, the RO4350B<sup>TM</sup> board has a dielectric constant of 3.66, and a dissipation factor of 0.0031 (which can be converted to the quality factor). In the data sheet, these values were tested at a frequency of 2.5 GHz. However, an assumption was made during the design process that these values would be approximately equivalent for the operational frequency selected.

Choosing the resonant frequency for the SRR required striking a compromise. Ideally, a higher resonant frequency would improve the quality factor, reducing power losses and making it more likely that a plasma discharge occurs. However, a frequency that is too high would increase power requirements required to drive the SRR. An additional drawback to using higher frequencies is that as seen in equation 4.1, increasing the frequency causes a decrease in the wavelength, which in turn reduces the size of the SRR. While this is not directly a problem, a smaller ring for the SRR would require significantly tighter manufacturing tolerances which in turn drive up the cost of production. Therefore, a target frequency of 500 MHz was chosen to strike a balance between the these factors.

Feeding this number into equation 4.1, the corresponding wavelength was 0.314 m. Since the circumference of the SRR is given as  $\lambda/2$ , this meant that the design had a circumference of 15.71 cm; which gives the SRR a radius of approximately 2.5 cm.

The next step was to determine the characteristic impedance. Conventionally, this impedance should be close to the value of the input impedance, which for power supply used was  $50 \Omega$ . As mentioned earlier in this chapter, three factors dictate the value of this parameter. The dielectric constant of the substrate was 3.66, a fixed value based on the material used. As stated in the

previous section, a thicker dielectric substate would be preferable. The RO4350B<sup>TM</sup> material came in a thickness of 0.5 mm, 0.8 mm, and 1.55 mm; with the costs increasing with thickness. Thus, as a compromise between the structural rigidity PCB and cost, a thickness of 0.8 mm was selected. By using the equations 4.3-4.6, a trace width of approximately 1.7 mm would produce a characteristic impedance of  $50.1 \Omega$ .

Finally using equation 4.2, the offset angle of the SRR was calculated. As from the datasheet, the dissipation factor of the RO4350B<sup>TM</sup> material is 0.0031. The reciprocal of this value was taken to determine the quality factor, which was 323. This would give a gap with an offset angle of 7.99. Again based on the simulations above, the ideal gap width was 240  $\mu\text{m}$ , however the minimum size drill hole size would be the limiting factor when manufacturing the device, hence the gap width was slightly increased to 250  $\mu\text{m}$ .

With these parameters known, the next stage was to create the PCB design. This was done using the open-sourced PCB design software called *KiCad*<sup>1</sup>. One benefit of using KiCad was the output files were natively supported by the PCB manufacturer used, *EuroCircuits*<sup>2</sup>.

An illustration of the final design can be seen in figure 4.6. As seen from the figure, four SRR designs were made. These were done to test various gap designs that could not be replicated using XOOPIIC simulations. These designs could be broken down into two categories: single versus multiple drill hole in the SRR gap; and the presence versus absence of ‘finger-like’ copper pours next to the SRR gap. The permutations of these categories resulted in the four designs, with a close up image of each shown in figure 4.7. All four designs used an SMA connector as the input source.

---

<sup>1</sup><https://www.kicad.org>

<sup>2</sup><https://www.eurocircuits.com>

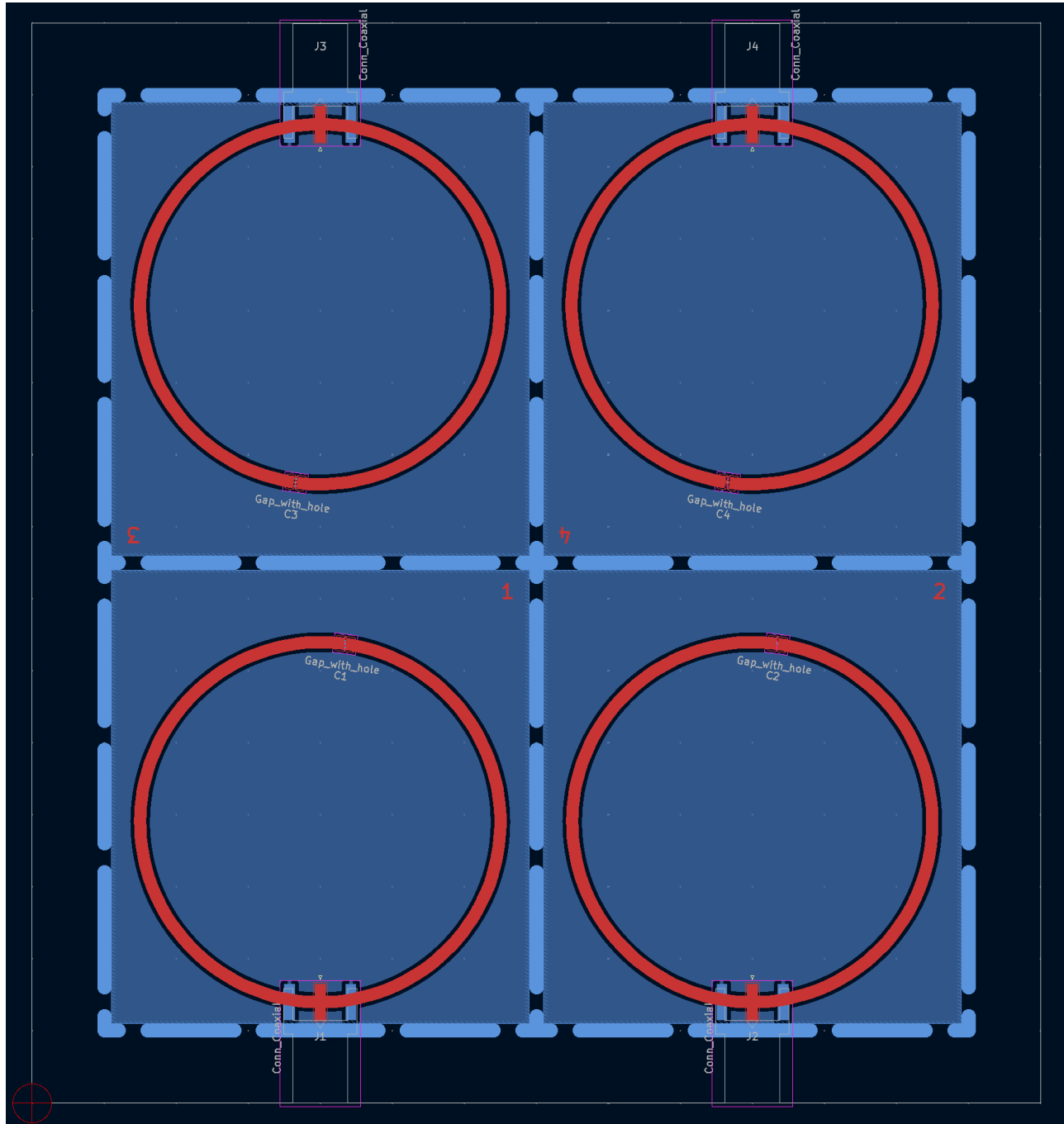


Figure 4.6: PCB schematic of SRR panels in the KiCad software suite.

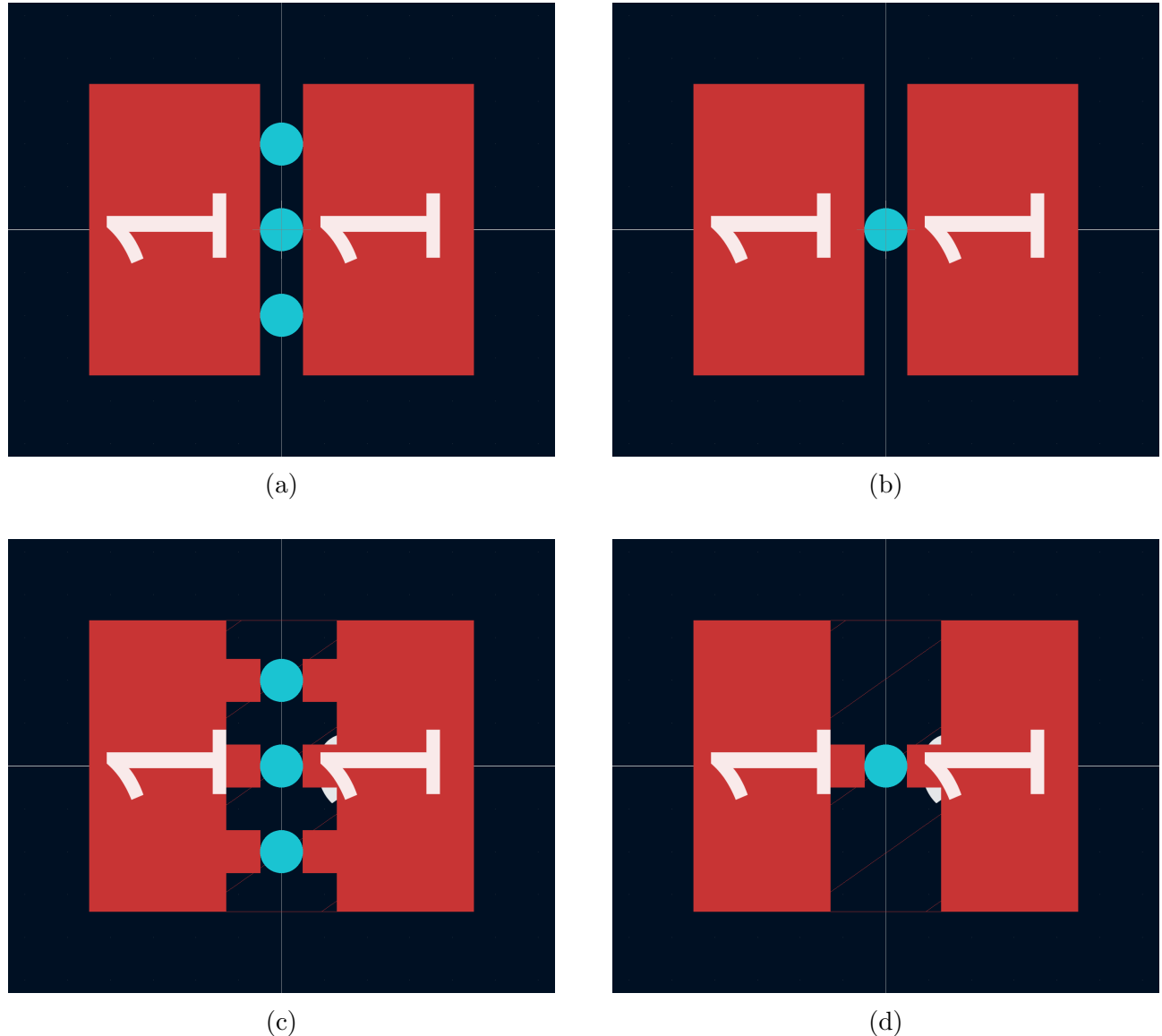


Figure 4.7: SRR gap designs with multiple holes (a, c) versus single holes (b, d). The designs in the lower two subfigures (c, d) have the presence of ‘finger-like’ copper pours next to the holes.

## 4.3 Testing

### 4.3.1 Scattering Parameters

Once the PCBs were manufactured, and the SMA connectors soldered on to the SRR panel, a comparison between the theoretical calculations of the SRR and its real world characteristics could be made. This was achieved best evaluating its *scattering parameters* (S-parameters) using a vector network analyser (VNA).

In essence, the S-parameters are a measurement of the transmitted and reflected power of a device under test, in this case the SRR, as a function of frequency. The output of this test is a description of the device in terms of amplitude and phase across a given sweep of frequencies. Since the SRR only had a single port, it only had one S-parameter, referred to as the  $S_{11}$  or the reflection coefficient. This is a ratio of the output voltage of the port to the input voltage going into the device.

For the test, the VNA was first calibrated then a sweep was performed between the frequencies of 100 MHz to 1 GHz. Since the SRR was designed to resonate at approximately 500 MHz, this should place a single largest peak at roughly the centre of the frequency range, and the broad range would also capture any shifts in the resonant frequency due to manufacturing tolerances.

Figure 4.8 shows the data from the  $S_{11}$  test, with the y-axis indicating the magnitude of attenuation (in decibels) at a given frequency. Readers will immediately notice the fact that there are two peaks in the SRR, not just one. The peaks have a central frequency of 554 MHz and 753 MHz respectively. The first of these peaks would be inline with the margin of error for the designed resonant frequency. The second peak on the other hand, represents some additional resonance in the SRR circuit. This could be introduced by a number of factors, such as SMA connector itself or the presence of gaps on the underside along the ground ring. While this second peak indicates a stronger resonance, as seen by the larger attenuation and higher quality factor, it is not possible to ignite a plasma at that frequency. This is because, as stated earlier in this chapter, the formation of the plasma is governed by the relationship between the

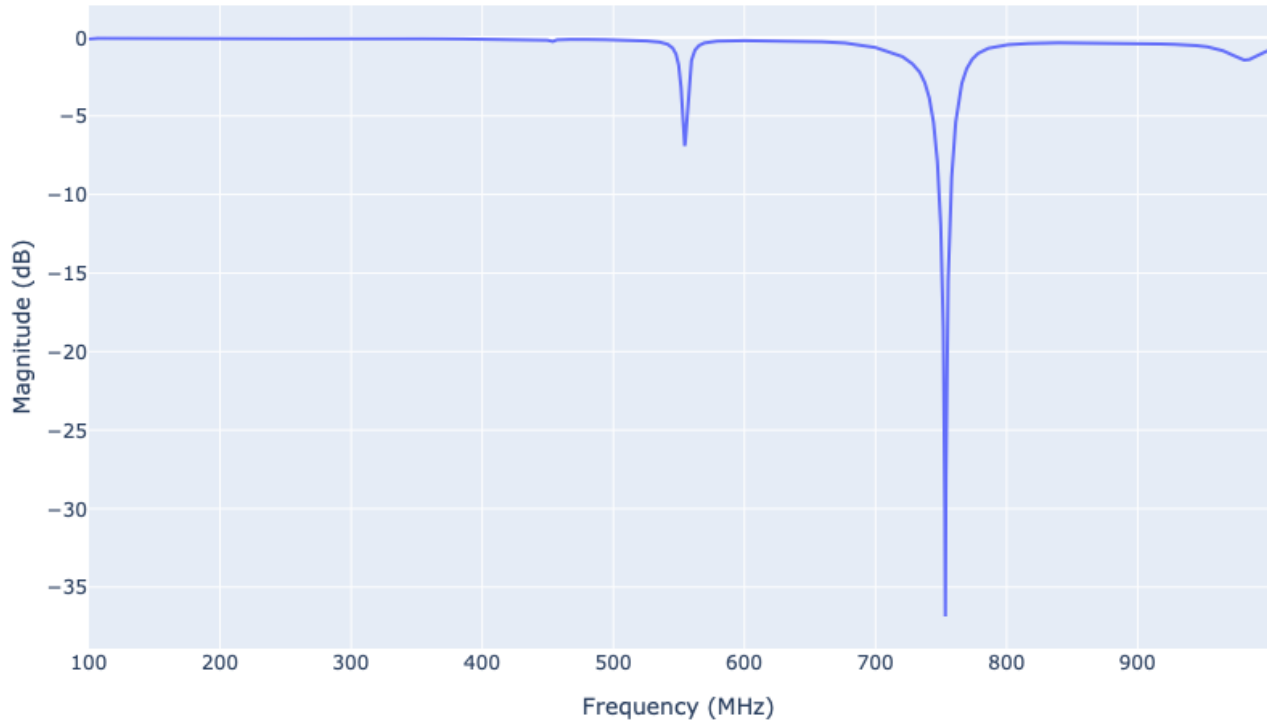


Figure 4.8: Reflection coefficient ( $S_{11}$ ) of SRR in dB.

wavelength of the input power and the circumference of the SRR.

As for first peak at 554 MHz, it appeared to have a much lower quality factor in the real world. This implies that the assumption made in the design phase regarding the dielectric constant and dissipation factor were incorrect. While this does not necessarily affect the plasma discharge, it does mean that a higher power is going to be required to ignite the plasma.

### 4.3.2 Experimental Setup

Once the true resonant frequency was determined, the next step was to setup the experiment. Note that this is not the final setup to be used for recirculating the gases, instead it was used to reliably ignite a plasma from the SRR in order to characterise it and understand its behaviour. An illustration of the setup is seen in figure 4.9.

In the setup, there are two mass flow controllers by MKS Instruments. For the time being, these are only controlling the flow of helium gas into the setup; the introduction of carbon dioxide

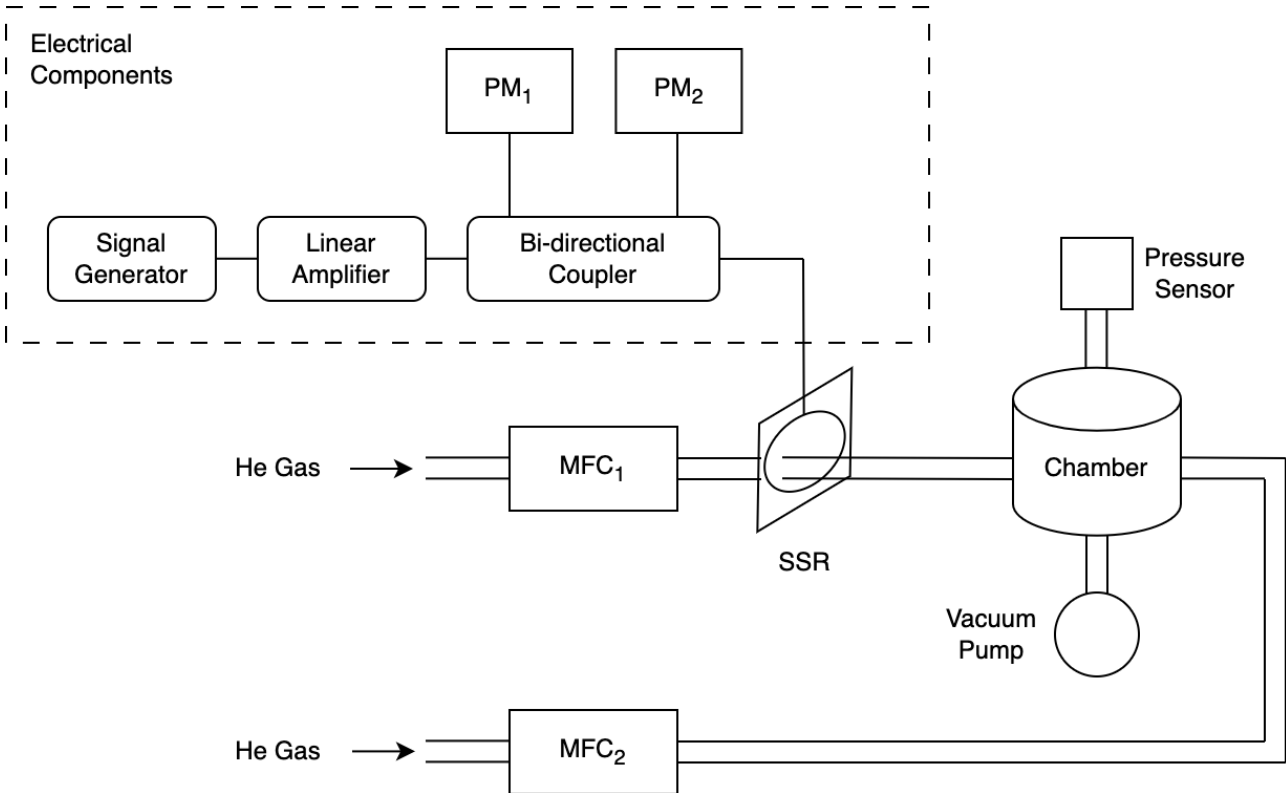


Figure 4.9: Schematic of experimental setup.

gas is discussed in the next chapter. The first one (MFC<sub>1</sub>) is positioned on the bottom side of the SRR, whilst the second one (MFC<sub>2</sub>) controls the flow to the chamber. The reason for two separate mass flow controllers is that the size of the aperture of the SRR is quite small (with a diameter of 0.25 mm), hence only using one controller to pressurise the entire apparatus at 760 Torr (which is one atmosphere) would take a long time. Thus, MFC<sub>2</sub> is used to maintain pressure the pressure of the chamber whilst MFC<sub>1</sub> maintains a flow of Helium through the gap of the SRR.

The SRR device is oriented so that the Helium flows from the bottom (i.e. the ground ring) to top; (i.e. the AC ring). This is because the plasma discharge occurs at the top of the ring, thus when used later in the epoxidation process, this is the side that is going to face the liquid co-reactant. A photographs of the plasma can be seen in figure 4.10.

In terms of the electronics, the the SRR is powered by a signal generator (Aim-TTi TGR2050), capable of generating frequencies up to 2 GHz, and a linear amplifier (Amplifier Research 50W1000A), with a maximum power output of 50 W. This is connected to a bi-directional cou-

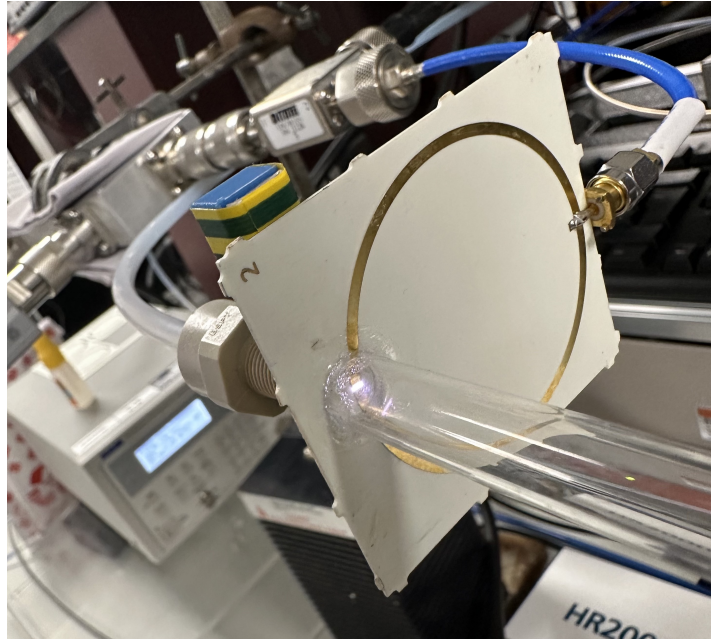


Figure 4.10: Photograph of plasma discharge in the gap of the SRR.

pler (Mini-Circuits ZGBDC20-33H-S+) to allow for the accurate measurement of the forward path and the reverse path of the microwave signals from the power supply and SRR respectively. These signals are monitored using a pair of USB power meters (Mini-Circuits PWR-SEN-4GHz, Mini-Circuits PWR-SEN-6LRMS-RC). One note regarding the power meters, the first power meter ( $PM_1$ ) has a maximum power input of 100 mW, whilst the second one ( $PM_2$ ) has a maximum reading of 10 mW. This is because, when the SRR is at resonance, only a small amount of signal is reflected back.

### 4.3.3 Plasma performance

Now that the SRR was connected to the setup, there may be a slight change in the resonant frequency due to coupling with the rest of the electronics. However, with the use of the bi-directional couplers and the power meters, it is possible to find the frequency of resonance of the overall setup. This is achieved by keeping the input power of the power supply fixed, but varying its frequency. This way, the reading of the forward wave would be constant, with the power of the reflected wave changing.

For this, the input power was kept at a constant 10 mW. This was chosen as it was a low

enough power to not ignite a plasma (which in turn would change the resonance characteristics of the SRR). As for the frequencies, a sweep was performed between 500 MHz to 600 MHz. The results of this can be seen in figure 4.11.

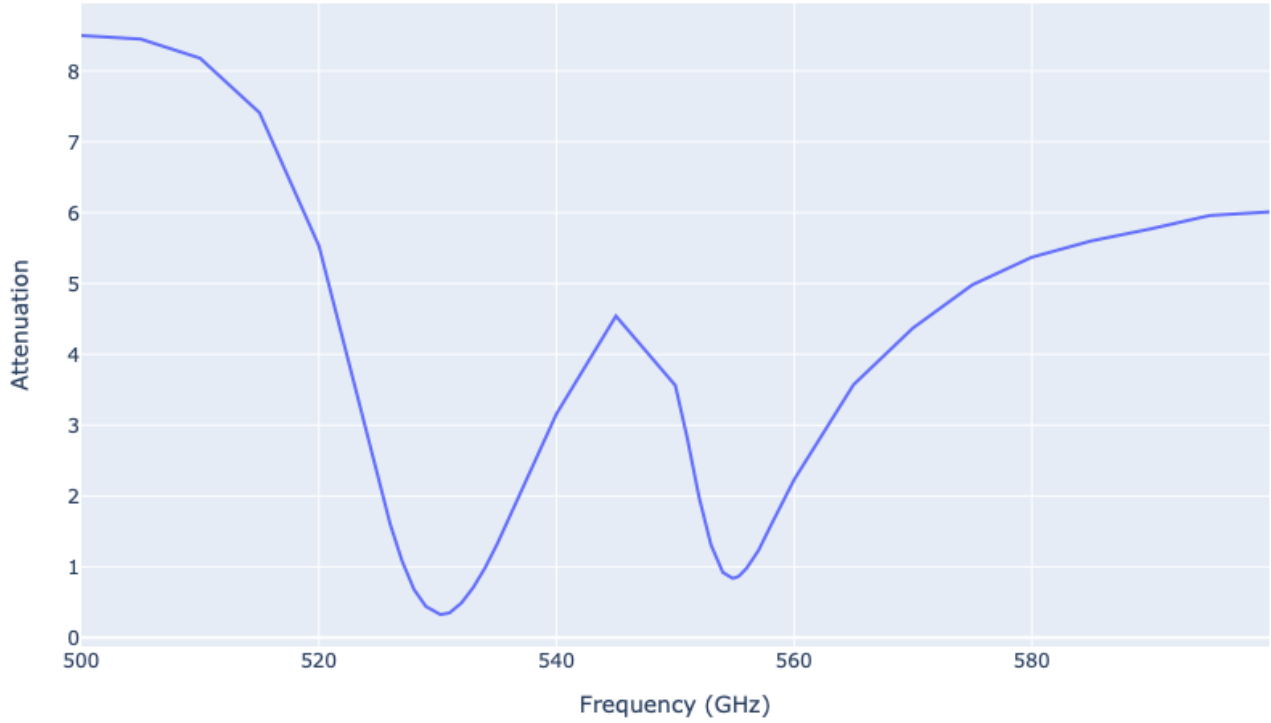


Figure 4.11: Reflection power of SRR when connected to the setup in mW.

Two dips can be seen in the data. These dips correspond to the frequencies that cause an attenuation in the SRR. As expected, a drop in return power can be seen at 554 MHz (more precisely, it is 554.8 MHz), which is inline with the S-parameters measurements. However, a second dip is seen at 530 MHz (530.4 MHz specifically). Notably, this drop of return power at 530 MHz is lower than that of the drop at 554 MHz; with the readings being 0.33 mW and 0.84 mW respectively. As such, it can be concluded that 530.4 MHz is resonant frequency of the SRR connected to the rest of the setup. This conclusion is backed up by the fact that the plasma only ignites at that frequency, and not at 554 MHz.

Once ignition was achieved, the next steps were to evaluate the performance of the plasma. The first thing to evaluate was the ignition power of the SRR. This is because, igniting plasma at higher pressures tends to be slightly more inefficient compared to lower pressures. Thus, the

ignition power was tested at various pressures to determine the minimum power required to get a plasma to form with the SRR.

To obtain this data, first the pressure of the chamber was fixed. Then input power to the SRR was increased gradually until the self-ignition of the plasma. The power value was noted, and the input power was reduced back to the minimum value and the process was repeated. In total, there were five power readings taken at each pressure to account for outliers. This data is shown in figure 4.12. Each point in the figure denotes the average ignition power at that pressure, with the error bars denoting the standard deviation in the data collected. Do note that x-axis of this graph was plotted in logarithmic scale.

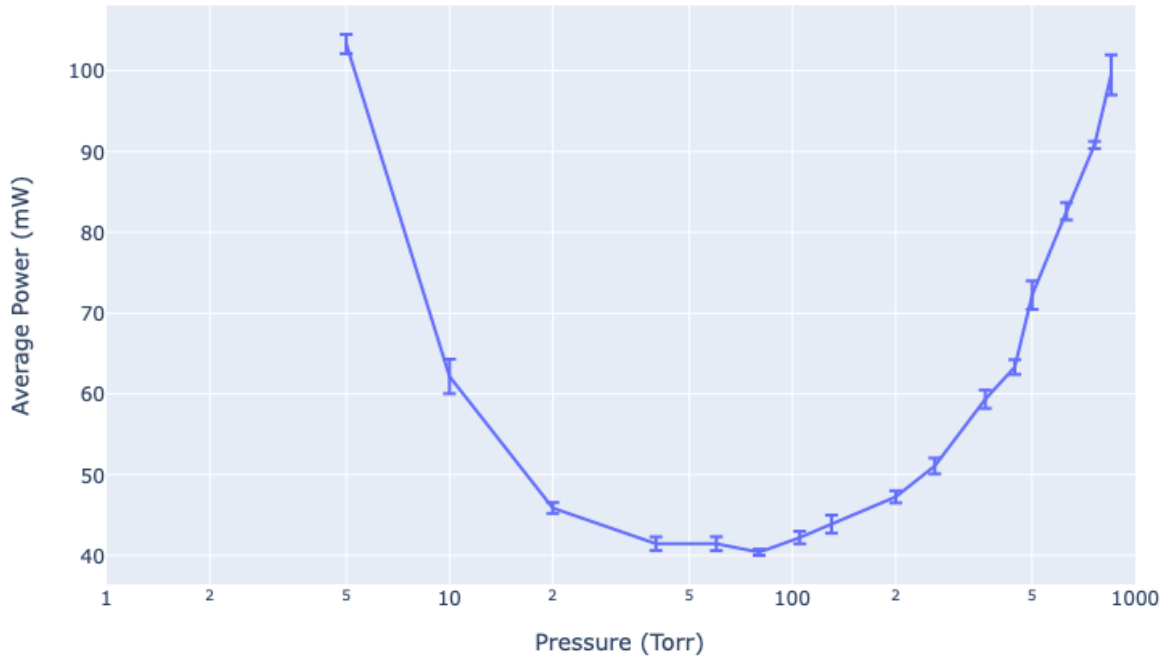


Figure 4.12: Ignition power of SSR, in mW, across a pressure range of 5 Torr to 850 Torr.

As seen by the graph, the minimum power required to ignite the plasma was just 40.4 mW. While this is fairly small, it could be better as the real world quality factor of the SRR was lower than anticipated. While this minimum ignition power was achieved at 80 Torr, the power remained relatively low across a broad range of pressures, ranging from 40 Torr to 105 Torr, with the ignition power hovering around 41-42 mW. As the pressure decreased below 40 Torr,

the ignition power required increased steeply up to a pressure of 5 Torr where the readings maxed out the range of the power meter. It is also important to note that at 5 Torr, while the plasma self-ignited, it did take significantly longer when compared to the ignition at other pressures. As for pressures above 105 Torr, the ignition power also increased, though at a much slower rate. At 760 Torr, the average power required to ignite the plasma was 90.8 mW. The testing was carried out past 760 to determine the upper bound pressure that a plasma could be ignited with the equipment in the setup; this value was at 850 Torr.

From the data in figure 4.12, it can be concluded that the most efficient way to ignite a plasma with this SRR would be to first pressurise the chamber to approximately 100 Torr. Then, once the plasma is ignited, the pressure can be increased back to 760 Torr.

# **Chapter 5**

## **Epoxidation Process**

# Chapter 6

## Gas recirculation

# Chapter 7

## Conclusion

# Appendix A

## Particle-in-Cell Simulations

Plasmas are complex non-linear systems and contain many unknown variables. Therefore, simplified models are often used to capture major physics of the system whilst ignoring details that can be considered negligible. There are several types of plasma models but the most commonly used methods are fluid description models and kinetic description models [54].

The fluid description method aims to generalise the plasma quantities, such as its density and velocity, by averaging them over a 2D or 3D region . This is achieved by numerically solving the fluid equations; obtained by utilising the velocity components of the Boltzmann equation [54]. Then, the electromagnetic fields are obtained by combining the fluid equations with Maxwell's equations.

In contrast, kinetic description models track the position and velocities of particles within the plasma, taking into account the electromagnetic forces acting on them. As a general rule of thumb, fluid models simulate the plasma behaviour over a macroscopic scale; whilst kinetic models highlight plasma behaviour at the microscopic level.

Particle-in-cell (PIC) simulations are a variant of kinetic description models that tend to be favoured because of its easy formulation. Real-world plasma systems contain a prodigious number of particles, which include electrons, ions, and the background neutral gas; thus, tracking all these particles would be immensely computationally taxing. PIC simulations partially solve

this by tracking so-called *super-particles* [55]. Each super-particle is scaled to represent a number of “real” particles. This scaling factor does not affect the trajectory of the super-particles as the motion of particles within a electromagnetic field are only governed by its mass to charge ratio (see the Newton-Lorentz expression in equation A.3) [55]. For the rest of this chapter, the term super-particle and particles are used interchangeably.

The PIC simulations discussed in this report are known as 2D-3v simulations, i.e. they are 2-dimensional in space but 3-dimensional in velocity. In these simulations, the particle properties (i.e. their position and velocity) are defined in continuous space within the simulation domain. However, the electromagnetic field values are only specified at fixed grid points. Therefore, intermediary steps are required to discretise charges and current densities onto the grid and also interpolation of forces by fields on the particles. These particles and fields are updated sequentially, with time being advanced in small discrete constant steps. An overview of this procedure can be seen in figure A.1 [56]. The rest of this chapter is dedicated to providing an overview of each process in the flow chart.

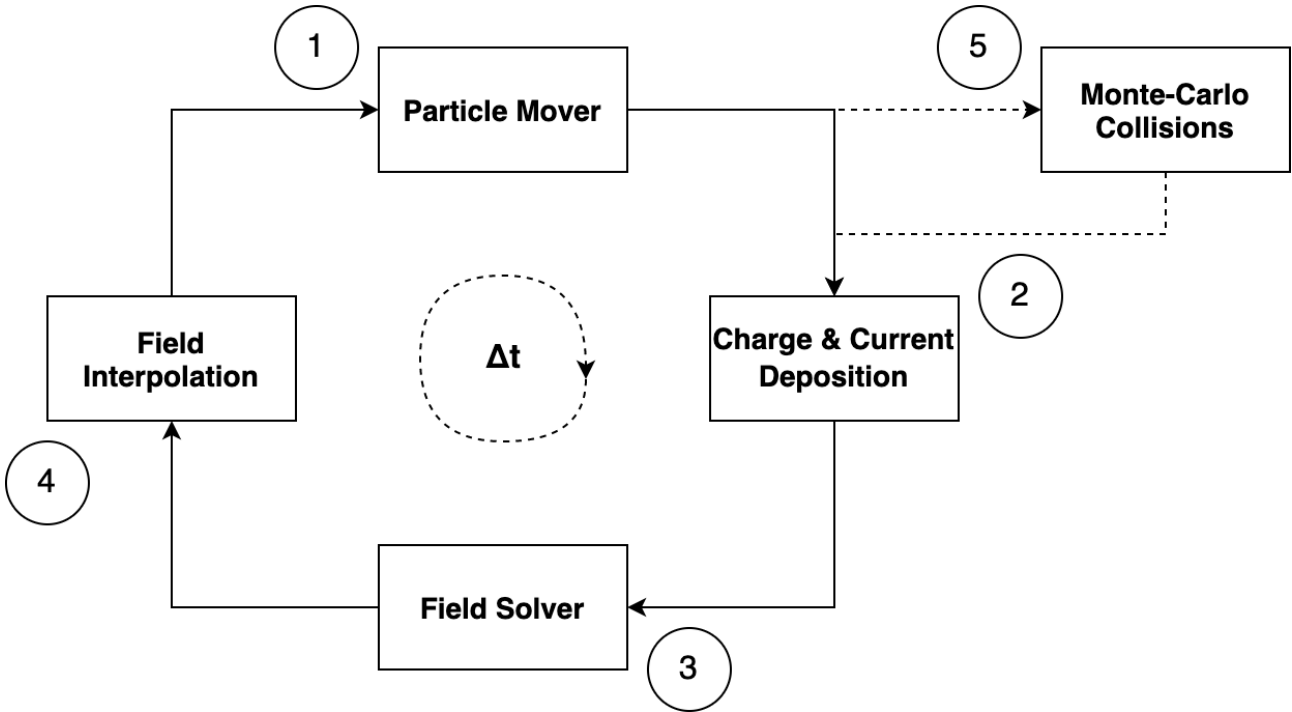


Figure A.1: Process flow of PIC simulations.

## A.1 Particle Mover

When first launching the PIC simulation, a random distribution of particle positions and velocities is initialised within the simulation domain. The acceleration of a particle is given by Newton's second law:

$$\frac{d\mathbf{v}}{dt} = \frac{\mathbf{F}}{m} \quad (\text{A.1})$$

The force acting on the particle is determined by the Lorentz force:

$$\mathbf{F} = q(\mathbf{E} + \mathbf{v} \times \mathbf{B}) \quad (\text{A.2})$$

where  $\mathbf{E}$  and  $\mathbf{B}$  are the electric and magnetic fields respectively, and  $q$  corresponds to the charge of the particle.

Combining equations A.1 and A.2 gives the Newton-Lorentz equation:

$$\frac{d\mathbf{v}}{dt} = \frac{q}{m}(\mathbf{E} + \mathbf{v} \times \mathbf{B}) \quad (\text{A.3})$$

As for the particles velocity, it is given by:

$$\frac{d\mathbf{s}}{dt} = \mathbf{v} \quad (\text{A.4})$$

In order to obtain the particle velocity and position, equations A.3 and A.4 have to be numerically integrated with respect to time using the *finite-difference method*; specifically the *leapfrog method* [57]. Thus, the new finite-difference forms of the respective equations are:

$$\frac{\mathbf{v}^{t+\frac{1}{2}} - \mathbf{v}^{t-\frac{1}{2}}}{dt} = \frac{q}{m}(\mathbf{E} + (\frac{\mathbf{v}^{t+\frac{1}{2}} - \mathbf{v}^{t-\frac{1}{2}}}{2}) \times \mathbf{B}) \quad (\text{A.5})$$

$$\frac{\mathbf{s}^{t+1} - \mathbf{s}^t}{dt} = \mathbf{v}^{t+\frac{1}{2}} \quad (\text{A.6})$$

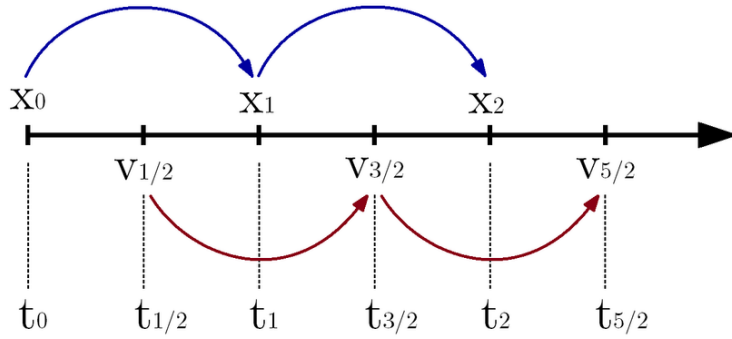


Figure A.2: Illustration of forward-difference and central-difference form [58].

Notice that the particle position is given by the *forward-difference form*, whereas its velocity is given by the *central-difference form*. This is done to conserve the energy of the dynamic system. An intuitive explanation for this is that when solving for the updated position of the particle, its average velocity should be used. Using either the initial or final velocities can result in the particle gaining energy if its accelerating, or losing energy if its decelerating. A visualisation of the difference can be seen in figure A.2.

To solve the Newton-Lorentz equation, the de-facto method used is the *Boris algorithm* [59] for its accuracy, speed, and simplicity. The method first redefines both velocity terms as:

$$\mathbf{v}^{t-\frac{1}{2}} = \mathbf{v}^- - \frac{q\mathbf{E}}{m} \frac{dt}{2} \quad (\text{A.7})$$

$$\mathbf{v}^{t+\frac{1}{2}} = \mathbf{v}^+ + \frac{q\mathbf{E}}{m} \frac{dt}{2} \quad (\text{A.8})$$

When substituted back into the the finite-difference Newton-Lorentz equation (equation A.5), this eliminates the electric field, resulting in an equation that expresses the rotation of the particle's velocity:

$$\frac{\mathbf{v}^+ - \mathbf{v}^-}{\Delta t} = \frac{q}{2m} (\mathbf{v}^+ + \mathbf{v}^-) \times \mathbf{B} \quad (\text{A.9})$$

Because it describes a rotation, it can be solved geometrically. Using the following 2D case seen in figure A.3, it can be determined that the angle through which the velocity rotates is:

$$\tan\left(\frac{\theta}{2}\right) = \frac{\mathbf{v}^+ - \mathbf{v}^-}{\mathbf{v}^+ + \mathbf{v}^-} = \frac{q\mathbf{B}}{m} \frac{\Delta t}{2} \quad (\text{A.10})$$

This angle can also be represented in vector form, referred to as  $\mathbf{T}$ . Using this vector form, a bisecting vector  $\mathbf{v}'$  can be obtained is parallel to the  $\mathbf{v}^+ + \mathbf{v}^-$  vector (the sum of the pre-rotation and post-rotation vector), and perpendicular to both the  $\mathbf{T}$  vector (the scaled magnetic field) and the  $\mathbf{v}^+ - \mathbf{v}^-$  vector (the difference between the post-rotational and pre-rotational velocity).

$$\mathbf{v}' = \mathbf{v}^- + \mathbf{v}^- \times \mathbf{T} \quad (\text{A.11})$$

Finally to obtain the  $\mathbf{v}^+ - \mathbf{v}^-$  vector, this intermediate vector  $\mathbf{v}'$  is combined with a new vector  $\mathbf{S}$  which can be thought of as a scaled version of vector  $\mathbf{T}$  seen in equation A.13.

$$\mathbf{v}^+ = \mathbf{v}^- + \mathbf{v}' \times \mathbf{S} \quad (\text{A.12})$$

$$\mathbf{S} = \frac{2\mathbf{T}}{1 + \mathbf{T}^2} \quad (\text{A.13})$$

Thus, in order to determine the new velocity of the particle:

1. First calculate the velocity of the particle over the first half time step using equation A.7.

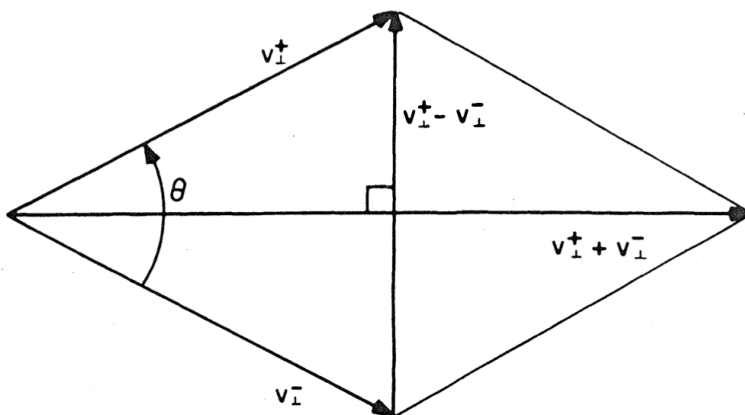


Figure A.3: Visualisation of velocity rotation from the Boris algorithm [59].

2. Then perform the full rotation of the velocity due to the magnetic field using equations A.11 and A.12.
3. Finally, calculate the velocity of the particle over the second half time step using equation A.8.

To obtain the particles new position, substitute the newly calculated velocity of the particle into equation A.6. Once calculated, the positions of each particle in the simulation can be updated.

## A.2 Charge and Current Deposition

Once the particles have been moved, their charge and current densities are discretised onto a the specified grid. The exact method of discretising these properties depends on the type of grid for the PIC simulation. The one described in this report is for a uniform 2D rectilinear grid, known as *bilinear interpolation* [60].

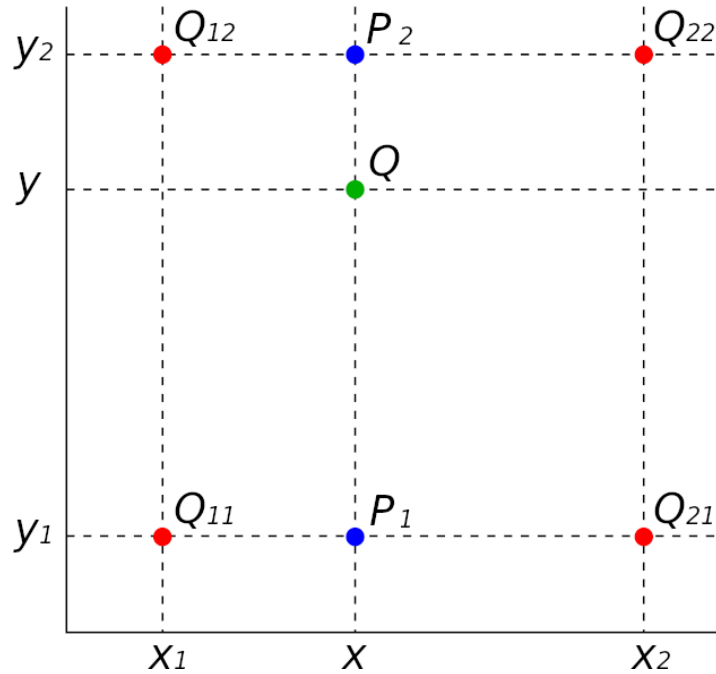


Figure A.4: Interpolation from the grid to the particles [61].

Consider the following case in figure A.4. The charge of the particle within the grid cell is distributed across the four vertices of the cell, called the *nodes*. The total charge experienced

by each node must equal to the charge of the particle, with nodes closest to the particle experiencing the greatest weight. This can be expressed as:

$$\begin{aligned} Q_{11} &= Q \frac{(x_2 - x)(y_2 - y)}{(x_2 - x_1)(y_2 - y_1)} \\ Q_{12} &= Q \frac{(x_2 - x)(y - y_1)}{(x_2 - x_1)(y_2 - y_1)} \\ Q_{21} &= Q \frac{(x - x_1)(y_2 - y)}{(x_2 - x_1)(y_2 - y_1)} \\ Q_{22} &= Q \frac{(x - x_1)(y - y_1)}{(x_2 - x_1)(y_2 - y_1)} \end{aligned} \quad (\text{A.14})$$

Intuitively, the weight of a node corresponds to the ratio of the area of the rectangle opposite (formed by the point of the particle and the point of the opposite node) and the total area of the cell.

Once the (weighted) charges at each node point has been calculated for all particles, the charge density of a node can be determined by summing the total charge on the node from all particles, then dividing by the area of the cell. This node area is typically given as  $(x_2 - x_1)(y_2 - y_1)$ , with the exception being nodes at the edges or corners of the simulation domain. With such cases, the resulting area is halved and quartered respectively.

A similar process is done to determine the current densities around a node. However, rather than just summing the charges, the total sum of the product between the particles charge and average velocity are taken.

### A.3 Field Solver

The field solver utilises the charge and current densities at the grid points to determine their corresponding electric and magnetic field values by solving Maxwell's equations. This report will only consider the electrostatic case and therefore will focus on the process of computing the electric field values.

Gauss's law dictates that the divergence of the electric field in a region is proportional to its

charge density:

$$\nabla E = \frac{\rho}{\varepsilon_0} \quad (\text{A.15})$$

The electric field is determined as the gradient of the electric potential, and by substituting that into the above equation results in Poisson's equation:

$$-\nabla^2 \phi = \frac{\rho}{\varepsilon_0} \quad (\text{A.16})$$

Considering a 2D case with a cartesian coordinate system, Poisson's equation can be rewritten as:

$$\frac{\partial^2 \phi}{\partial x^2} + \frac{\partial^2 \phi}{\partial y^2} = -\frac{\rho}{\varepsilon_0} \quad (\text{A.17})$$

In order to solve Poisson's equation in a discretised domain, the finite-difference method is employed. Specifically using the central-difference, the resulting approximation seen in equation A.18 is produced, which is classed as second order accurate.

$$\frac{\phi_{x+\Delta x, y} - 2\phi_{x, y} + \phi_{x-\Delta x, y}}{\Delta x^2} + \frac{\phi_{x, y+\Delta y} - 2\phi_{x, y} + \phi_{x, y-\Delta y}}{\Delta y^2} = -\frac{\rho}{\varepsilon_0} \quad (\text{A.18})$$

There are several method to solve such an equation numerically. An overview of method used by XOOPIIC (simulation program used in this work, see chapter 4) is described below.

The Poisson equation is classed as an elliptic partial differential equation, which can be written in this form [62]:

$$\mathcal{L}u = \lambda \quad (\text{A.19})$$

where  $\mathcal{L}$  is the elliptical operator and  $\lambda$  is the source term.

It is then possible to rewrite this as a diffusion equation (i.e. with respect to time):

$$\frac{\partial u}{\partial t} = \frac{\partial^2 u}{\partial x^2} + \frac{\partial^2 u}{\partial y^2} - \lambda \quad (\text{A.20})$$

which is equivalent since as  $t \rightarrow \infty$ ,  $\frac{\partial u}{\partial t} \rightarrow 0$ .

Therefore, equation A.20 can be expressed as a diffusion equation in the finite-difference form:

$$\frac{\phi_{x,y}^{t+\Delta t} - \phi_{x,y}^t}{\Delta t} = \frac{\phi_{x+\Delta x,y} - 2\phi_{x,y} + \phi_{x-\Delta x,y}}{\Delta x^2} + \frac{\phi_{x,y+\Delta y} - 2\phi_{x,y} + \phi_{x,y-\Delta y}}{\Delta y^2} + \frac{\rho}{\varepsilon_0} \quad (\text{A.21})$$

From this, a technique known as the *alternating-direction implicit* (ADI) method can be employed. In essence, the ADI method utilises a concept known as operator splitting, wherein the  $\frac{\partial^2 \phi}{\partial x^2}$  and  $\frac{\partial^2 \phi}{\partial y^2}$  terms can be decoupled, then each can be solved by iterating over half a time step. So for the first half time step, a pass is performed along the  $x$  direction; then at the second half time step, a pass is performed along the  $y$  direction as illustrated in figure A.5.

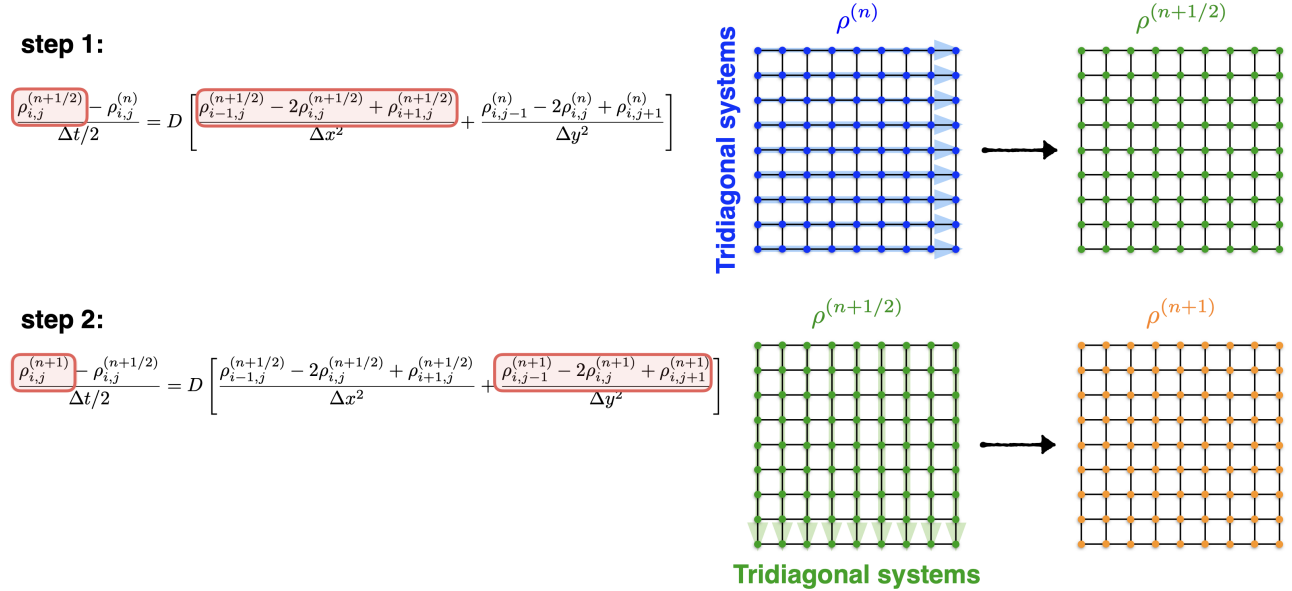


Figure A.5: Illustration of ADI method [63].

The benefit of this method is that rather than solving a large sparse matrix of a 2D system, a set of two independent 1D systems can be solved. These 1D systems can be arranged as a tridiagonal matrix, which can be efficiently solved using the *Thomas algorithm* [64].

Once the Poisson equation is solved and the potentials at the grid determined, the electric field

can be calculated again by the finite difference method. As the electric field is a vector, it needs to be calculated both along the direction of the  $x$ -axis and  $y$ -axis. Considering only the direction along the  $x$ -axis, equation A.22 can be used. For the case of a boundary, equation A.23 should be used instead.

$$E_x^{i,j} = \frac{\phi_{i+\Delta x,j} - \phi_{i-\Delta x,j}}{2\Delta x} \quad (\text{A.22})$$

$$E_x^{i,j} = \frac{\phi_{i+\Delta x,j} - \phi_{i,j}}{\Delta x} \quad (\text{A.23})$$

## A.4 Field Interpolation

The interpolation of the electromagnetic field values on the particles is also performed using bilinear interpolation, however the reverse method to that done for the charge and current deposition. Therefore the electric field experienced by the particle is given by the contribution of the electric field vectors at each grid point.

Again, the general case seen in figure A.4 can be used. Here first step is to determine two intermediate points  $P_1$  and  $P_2$ :

$$P_1 = Q_{11} \frac{x_2 - x}{x_2 - x_1} + Q_{21} \frac{x - x_1}{x_2 - x_1} \quad (\text{A.24})$$

$$P_2 = Q_{12} \frac{x_2 - x}{x_2 - x_1} + Q_{22} \frac{x - x_1}{x_2 - x_1} \quad (\text{A.25})$$

Then, interpolate to the point of the particle  $Q$ :

$$Q = P_1 \frac{y_2 - y}{y_2 - y_1} + P_2 \frac{y - y_1}{y_2 - y_1} \quad (\text{A.26})$$

Thus for the fields, the variables  $Q$  would be replaced with the electric field vectors and the magnetic field vectors respectively. This process is repeated for all particles and the new electromagnetic field values are used in the particle mover for the next time step.

## A.5 Monte-Carlo Collisions

Steps 1-4 in figure A.1 are used to simulate collisionless plasma systems, where the charge particles kinetics are governed by magnetic interactions. However, when elastic and inelastic collisions between particles cannot be ignored, an additional step is sandwiched between steps 1 and 2 to account for this.

This is known as the *Monte-Carlo collision* (MCC) method, and it describes the collisions between the particles in a probabilistic fashion [65]. To start, the particles are evaluated for collisions. If a collision occurs, the particle velocity is updated in lieu with the type of collision. One potential downside to using the MCC method is that source particles collide with a target “cloud”, which is not a simulated particle. However, in practice the density of the background is significantly larger than the number of charged species being simulated, so this trade off is acceptable.

Determining if each and every particle in the simulation undergoes a collision can be very computationally expensive, as this requires the computation of each particles kinetic energy and their corresponding collision cross sections. Therefore, a computational trick is employed by adding an artificial collision term. The cross section of this term is chosen to force the total collision frequency for each species to be uniform and independent of the kinetic energy of the particle. This is called the *null collision* [65], which is illustrated in figure A.6.

From this, the portion of particles that should undergo a collision can be determined by the following expression [66]:

$$P(t) = 1 - e^{-\nu \Delta t} \quad (\text{A.27})$$

where  $\nu$  is the maximum of the sum of all collision frequencies. This can be expressed mathe-

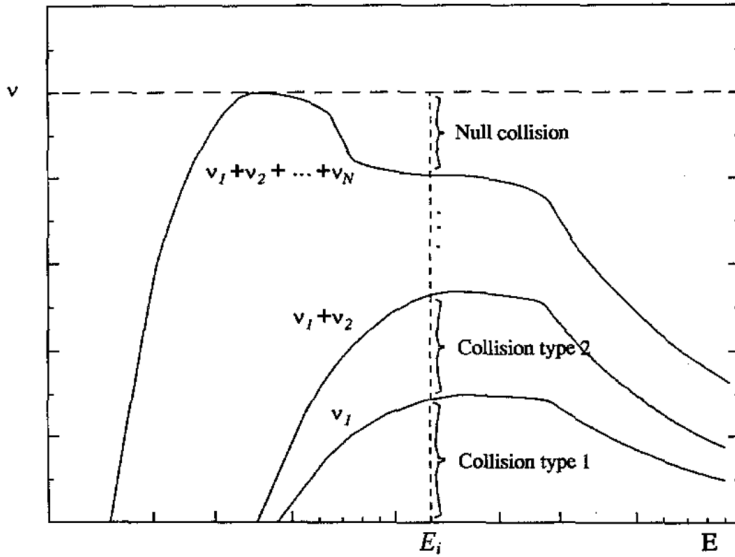


Figure A.6: Addition of null collision to produce a constant collision frequency across all energies [66].

matically as:

$$\nu = n_g \cdot \max(\sigma_{total}, v) \quad (\text{A.28})$$

where  $n_g$  is the neutral gas density (which can be assumed to be constant),  $\sigma_{total}$  is the total cross section from all collisions modelled (not including the null collision), and  $v$  is the relative speed between the colliding particle and the target.

Once the number of particles that experience collisions has been determined, particles are randomly picked from the population of simulated particles. This way, the kinetic energy of only a small subset of particles from the pool will be determined, making the simulation more efficient. Once a particle has been chosen and its kinetic energy calculated, a random number between  $[0, 1]$ , called  $R$ , is selected. This is used to determine the collision type for the particle, as a function of the value of  $R$ , as shown by table A.1.

Table A.1: Determining the type of collision based on the value of  $R$  [66].

	$R \leq \nu_1/\nu$	Collision Type 1
$\nu_1/\nu <$	$R \leq (\nu_1 + \nu_2)/\nu$	Collision Type 2
	$\vdots$	
$(\nu_1 + \nu_2 + \dots + \nu_n)/\nu <$	$R$	Null Collision

If the collision type selected is a null collision, then it is treated as no collision occurred.

# Appendix B

## XOOPIC

The PIC simulation program used in this project is called *X11 object-oriented particle-in-cell* (XOOPIC). It is a C/C++ based program that simulates 2D plasma systems. It was originally developed in the 1990s by the Plasma Theory and Simulation Group from the University of California at Berkley [53]. The code base was subsequently forked by the Plasma and Pulsed Power Group at Loughborough University, and improved upon to include additional features and output diagnostics for analysis.

### B.1 Overview

XOOPIC is primarily a command-line-interface (CLI) program but support X11 windowing to visualise certain diagnostics in real time. Some examples of these real time diagnostics include: average kinetic energies of the particles, phase-space plots of the position and velocities of the various particle species, and the electric field vectors at the simulation grid. While important for determining the behaviour of the plasma system, running the simulation with these windows does significantly reduce its performance. Therefore, XOOPIC's in-built visualisations are primarily used to observe the snapshot behaviour of the simulated system, whilst any diagnostic information required for further analysis is typically written into output files.

Despite not running with X11 windowing, running these simulations continuously takes a long

period of time (typically on the order of days to weeks) before they settle into a steady state. This is because the simulations have to be run at very small time steps in order to be stable (see section 4.1.2).

### B.1.1 Remote Server

Due to this long simulation time, running XOOPIIC simulations continuously on a local machine are just not feasible. Instead, simulations are run remotely on Loughborough University’s high performance servers via *secure shell* (SSH). Typically, multiple simulations are run concurrently in order to test various model parameters.

There are several risks associated with running simulations using a remote server. The first being that if (and when) the connection between the client and the server is severed, the simulations will be killed by the server. This problem can be alleviated with the use of terminal multiplexors, such as *GNU Screen*<sup>1</sup>. This allows for the creation of multiple pseudo-terminal sessions that run in the background. Once created, the client is free to attach and detach sessions without the need for an uninterrupted connection to the server.

A broken client-server connection is not the only way a simulation can be terminated. Some others include unexpected server restarts, power outages, or overuse of server resources due to memory leaks. In such cases, the simulation can be resumed using XOOPIIC’s dump files (also referred to as restart files). These files are essentially periodic saves of the simulations and can be used to restart the simulation from the last save point if the need arises. The save interval between dump files is set when starting the simulation. Though tempting to set this interval as small as possible in order to mitigate any data loss, generating these files is very expensive computationally as it involves writing most of the simulation variables onto disk. Thus, the dump file interval are set in the neighbourhood of hundreds of thousands of time steps.

---

<sup>1</sup><https://www.gnu.org/software/screen/>

### B.1.2 Input Files

The parameters for XOOPICTM’s simulations are set using an input file. This is simply a custom formatted text file, with a pseudo-JSON-like structure. The input file is divided into three sections: headers, variables, and region. The first two sections are for the user’s benefit, describing the simulation and the parameter values used respectively.

The region section however is where the true simulation parameters are specified. It can be further sub-divided into multiple subsections. The list of all possible subsections is vast, though a typical PIC simulation includes:

- **Grid** where the dimensions of the plasma device are specified, either in cylindrical or cartesian geometry.
- **Control** where the control parameters such as the size of the time step or a flag to use a specific field solver are set.
- **Species** which state parameters of the particle species being simulated, for example its mass and charge.
- **MCC** that determine the collision characteristics of the plasma based on the background gas pressure and temperature. The collisions can also be turned off outright.
- **Load** that establishes the region in which the particle species are loaded.
- **Diagnostic** which as the name suggests extracts the various diagnostic information and saves them to an output file.

The other subsections not listed are the various boundary parameters. The usage of these parameters will vary based on the type of device being simulated. Some examples of boundary parameters include: a grounded boundary, a current source, and a dielectric boundary.

When constructing the input files, care must be taken to ensure that the grid size (within the grid subsection) and the time step (within the control subsection) obey a set of conditions so that the simulation is stable.

The grid size of the simulation,  $\Delta x$  and  $\Delta y$  should adhere to the equation [57]:

$$\Delta x < 3.4\lambda_D \quad (\text{B.1})$$

where  $\lambda_D$  is the Debye length. This is to ensure that the electric fields in the sheath can be resolved.

As for the time step,  $\Delta t$ , it should be able to resolve the plasma oscillations, thus should satisfy the equation [67]:

$$\Delta t < 0.2\omega_{pe}^{-1} \quad (\text{B.2})$$

where  $\omega_{pe}$  is the plasma frequency. Note, this condition is only valid for electrostatic plasma simulations.

## B.2 Improvements

During the course of this project, several improvements were made to XOOPIIC. This primarily included bug fixes, but also the inclusion of a new boundary parameter (within the region section) called the *Circuit* boundary.

### B.2.1 Motivation

XOOPIIC previously had two types of (traditional) input source boundaries. An ideal voltage source, known as the *Equipotential* boundary; and an ideal current source, called the *Current Source* boundary.

With the Equipotential boundary, the simulation always keeps the potential at the boundary equal to the source voltage specified in the input file. This has the issue where there are no maximum or minimum bounds for current through the boundary. Thus, theoretically the current through the boundary can grow exponentially to infinity. In practice however, the simulation

simply becomes unstable and crashes. It is also possible for this current to exceed the rated current of the intended power supply to be used.

Likewise with the Current Source boundary, the simulation attempts to keep the current across the boundary at a constant specified value; despite the potential at the boundary. And in practice, it is possible that the potential produced by the simulation exceeds the voltage that can be delivered by the power supply.

Hence, in order to accurately simulate a “real world” power supply, the Circuit boundary was introduced. This boundary represents the configuration of an ideal voltage source with a resistor attached in series. An illustration of this can be seen in figure B.1. The one significant assumption with this boundary is that the circuit shares the same ground plane as the rest of the plasma device being simulated, which is normally the case.

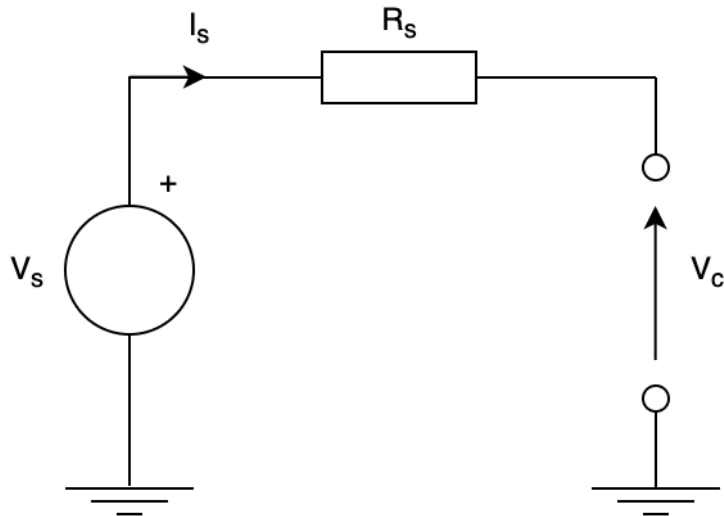


Figure B.1: Illustration of circuit boundary.

By adding the series resistor, in effect the maximum voltage and current across the boundary has been limited. As seen in figure B.2, the maximum voltage is obtained when the simulated device is an open circuit. As for the maximum current, it is achieved when the simulated device behaves as a short circuit. Thus the potential of the Circuit boundary can be given by:

$$V_c = V_s - I_s R_s \quad (\text{B.3})$$

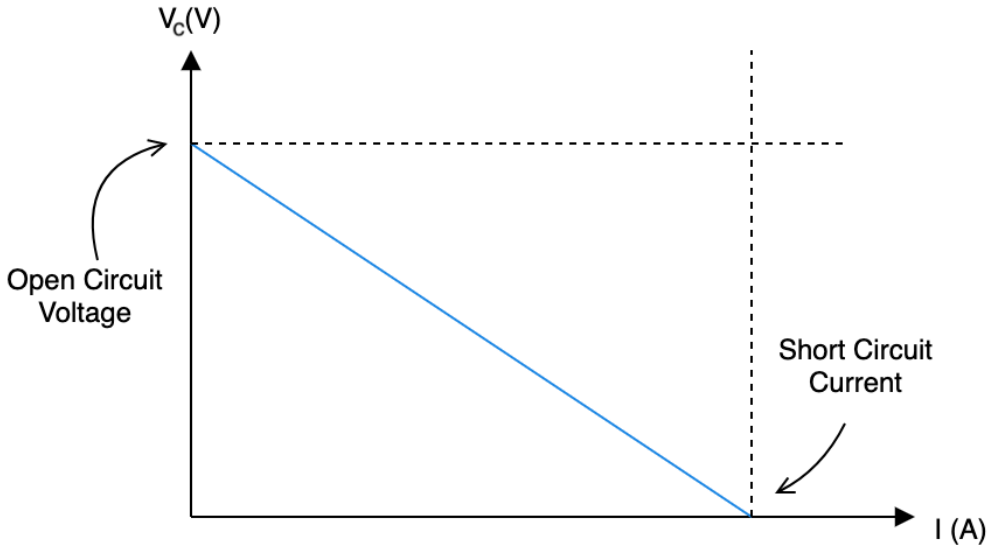


Figure B.2: Voltage-current relationship of circuit boundary.

### B.2.2 Methodology

As mentioned previously, XOOPIIC has the capability of performing simulations in cartesian geometry or cylindrical geometry. Hence an implementation was required for both geometry types. For this report, a general solution based on [68, 69] is first described, followed by the specific coefficient values required in either geometry.

#### General Solution

A case for the Circuit boundary shown in figure B.3. The points represent an arbitrary fixed grid, with grid points labelled  $i$  and  $j$  that correspond to the relative positions along the horizontal and vertical directions respectively. The boundary itself is represented by the vertical line, placed along the left most grid points, where  $i = 0$ .

The potential at each grid point that intersects the boundary is first taken, then these values are averaged to give the potential of the overall Circuit boundary. For a given point along the boundary, the potential can be computed using Gauss's law.

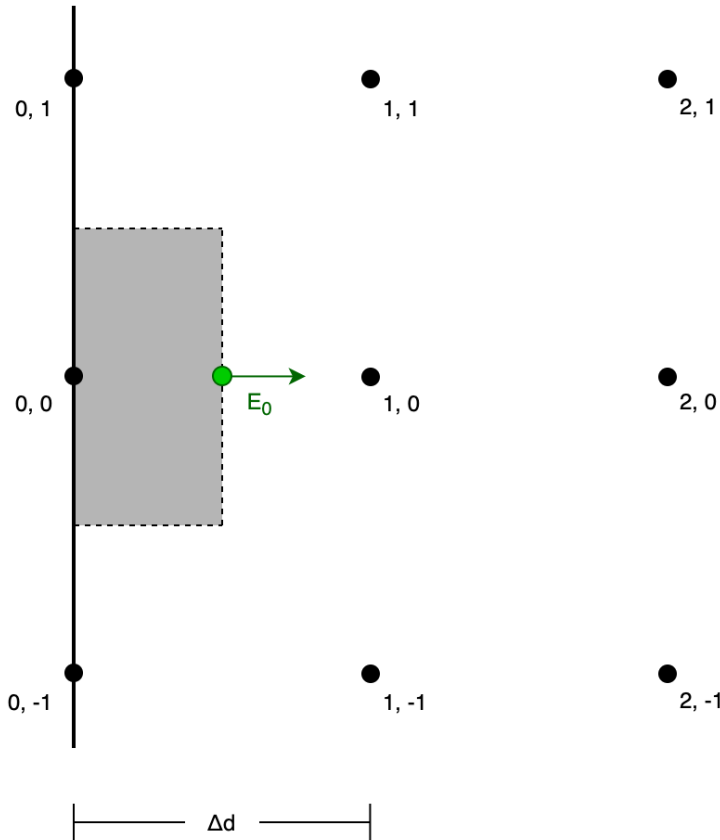


Figure B.3: Illustration of a circuit boundary along a fixed grid.

The expression for a Gaussian pillbox (shown by the dashed line in figure B.3) is:

$$\oint_S E \cdot dS = \frac{Q}{\epsilon_0} \quad (\text{B.4})$$

where  $Q$  is the charge enclosed by said pillbox. This charge can be expressed as a sum of the volume charge within the pillbox and the surface charge at the boundary:

$$Q = \oint_V \rho \cdot dV + \oint_S \sigma \cdot dS \quad (\text{B.5})$$

Combining equations B.4 and B.5, then integrating over their respective areas and volumes results in the expression:

$$E \cdot A_1 = \frac{1}{\epsilon_0} (\rho \cdot V + \sigma \cdot A_2) \quad (\text{B.6})$$

Note that there are two different areas produced: one related to the surface charge density along the boundary,  $A_2$ ; and one related to electric field out of the pillbox,  $A_1$ . The values of

these terms depend on the geometry used.

The electric field can be expressed in terms of the potential difference:

$$\mathbf{E} = -\nabla\phi \quad (\text{B.7})$$

Thus, the forward-difference method can be used to determine the electric field of the pillbox seen in figure B.5.

$$\frac{\phi_0 - \phi_1}{\Delta d} \cdot A_1 = \frac{1}{\varepsilon_0}(\rho \cdot V + \sigma \cdot A_2) \quad (\text{B.8})$$

An additional note regarding equation B.8, the term  $\Delta d$  denotes the distance between the grid points. Similarly to the area and volume terms, this value depends on the geometry used.

As explained in chapter 3, the volume charge densities of particles within PIC simulations are discretised onto the grid using bilinear interpolation. This means the the volume charge of the pillbox is known at the at the grid. Therefore, the only unknown term on the RHS of equation B.8 is the surface charge density.

This can be determined using Kirchoff's current law in the circuit shown in figure B.1:

$$\frac{d\sigma}{dt} = J_{cond} + J_{conv} \quad (\text{B.9})$$

Equation B.9 can be expressed numerically using the backwards-difference method. Additionally, the conduction and convection current density can expressed in terms of their charges, eliminating the  $dt$  terms on both sides.

$$\sigma^t - \sigma^{t-\Delta t} = \frac{1}{A_2} (Q^t - Q^{t-\Delta t} + Q_{conv}) \quad (\text{B.10})$$

The variables  $\sigma^{t-\Delta t}$  and  $Q^{t-\Delta t}$  represent quantities determined in the previous time step, thus should be known. Supposing it is the start of the simulation where  $t = 0$ , they can be simply initialised to zero.  $Q_{conv}$  represents the charge deposited onto the boundary by particles since the previous time step. Hence the only unknown term on the RHS of equation is the conduction

charge at the current time step,  $Q^t$ .

This conduction charge can be determined using Kirchoff's voltage law (also expressed in equation B.3, though in a slightly different form):

$$\phi_0 = V_s - \frac{dQ}{dt} \cdot R_s \quad (\text{B.11})$$

The derivative term can again be solved numerically using the backwards-difference. However unlike the other equations, a second order difference is used here to provide a better approximation of the charge. This second order backwards-difference is given as:

$$\frac{dQ}{dt} = \frac{3Q^t - 4Q^{t-\Delta t} + Q^{t-2\Delta t}}{2\Delta t} \quad (\text{B.12})$$

Combining equations B.11 and B.12 provides a new expression for the conduction charge,  $Q^t$ :

$$Q^t = \frac{V_s - \phi_0 - (\alpha_1 Q^{t-\Delta t} + \alpha_2 Q^{t-2\Delta t})}{\alpha_0} \quad (\text{B.13})$$

where  $\alpha_0 = \frac{3}{2} \frac{R_s}{\Delta t}$ ,  $\alpha_1 = 2 \frac{R_s}{\Delta t}$ , and  $\alpha_2 = \frac{1}{2} \frac{R_s}{\Delta t}$  are constants to simply the expression.

Using equation B.13, a new surface charge density expression can be determined:

$$\sigma^t - \sigma^{t-\Delta t} = \frac{1}{A_2} \left( \frac{V_s - \phi_0 - (\alpha_1 Q^{t-\Delta t} + \alpha_2 Q^{t-2\Delta t})}{\alpha_0} - Q^{t-\Delta t} + Q_{conv} \right) \quad (\text{B.14})$$

This in turn can be combined with equation B.8 from Gauss's law to give the expression:

$$\frac{\phi_0 - \phi_1}{\Delta d} \cdot A_1 + \frac{\phi_0}{\alpha_0 \varepsilon_0} = \frac{1}{\varepsilon_0} \left( \rho \cdot V + \sigma^{t-\Delta t} \cdot A_2 + \left( \frac{V_s - K^t}{\alpha_0} - Q^{t-\Delta t} + Q_{conv} \right) \right) \quad (\text{B.15})$$

where  $K^t = \alpha_1 Q^{t-\Delta t} + \alpha_2 Q^{t-2\Delta t}$ . Note, that the unknown terms ( $\phi_0$  and  $\phi_1$ ) have been rearranged to the LHS of the equation.

Typically, the coefficients in equation B.15 can then be fed into the field solver to determine the potential of all grid points. However in XOOPIIC, the grid potentials of each boundary

within the simulation are individually computed before the simulation begins. Then at each time step, the overall potential is determined by summing the predetermined potential induced by the individual boundaries via superposition, and adding the potential due to space charges (from the particles). This approach does not necessarily speed up the computation of the field solver, however it does decouple the boundary code from the field solver code; making it easier to implement new boundaries.

Because of this pre-computation, equation B.15 can be simplified by specifying  $\phi_1 = c_1\phi_0$ , where  $c_1$  is the ratio of  $\phi_1/\phi_0$ . Hence, the general solution for a circuit boundary can be given as:

$$\phi_0 \left( (1 - c_1)A_1 + \frac{\Delta d}{\alpha_0 \varepsilon_0} \right) = \frac{\Delta d}{\varepsilon_0} \left( \rho \cdot V + \sigma^{t-\Delta t} \cdot A_2 + \left( \frac{V_s - K^t}{\alpha_0} - Q^{t-\Delta t} + Q_{conv} \right) \right) \quad (\text{B.16})$$

## Cartesian Geometry

There are two possible orientations for the Circuit boundary for the cartesian geometry: along (or parallel to) the  $x$ -axis, or along the  $y$ -axis. Therefore, the variables seen in the left most column of table B.1 should be replaced by their values in the given orientation of the Circuit boundary.

Table B.1: Circuit boundary variables for cartesian geometry.

Variables	Along $x$ -axis	Along $y$ -axis
$\Delta d$	$\Delta y$	$\Delta x$
$A_1$	$\Delta x \Delta z$	$\Delta y \Delta z$
$A_2$	$\Delta x \Delta z$	$\Delta y \Delta z$
$V$	$\Delta x \Delta y \Delta z$	$\Delta y \Delta x \Delta z$

When operating in the cartesian coordinate system, the two area terms  $A_1$  and  $A_2$  are identical regardless of the orientation.

## Cylindrical Geometry

The two possible orientations for a cylindrical geometry are: along the r-axis, or along the z-axis. However, unlike the cartesian geometry where  $A_1$  always equals  $A_2$  for both orientation, this only holds for the case where the Circuit boundary is along the r-axis. For the case along the z-axis,  $A_1$  and  $A_2$  are distinct.

The terms for a given orientation of the Circuit boundary in cylindrical geometry can be seen in table B.2.

Table B.2: Circuit boundary variables for cylindrical geometry.

Variables	Along $z$ -axis	Along $r$ -axis
$\Delta d$	$\Delta r$	$\Delta z$
$A_1$	$2\pi r_{i+0.5\Delta r} \Delta z$	$\pi(r_{j+0.5\Delta r}^2 - r_{j-0.5\Delta r}^2)$
$A_2$	$2\pi r_i \Delta z$	$\pi(r_{j+0.5\Delta r}^2 - r_{j-0.5\Delta r}^2)$
$V$	$\pi(r_{i+0.5\Delta r}^2 - r_i^2) \Delta z$	$\frac{1}{2}\pi(r_{j+0.5\Delta r}^2 - r_{j-0.5\Delta r}^2) \Delta z$

### B.2.3 Validation

The validation for the Circuit boundary was done in two parts. The first was a test case without particles, which was then followed by one with particles. The former was used to evaluate the accuracy of the boundary calculations itself, without the computation from particles (i.e. the discretisation of the volume charge densities or the count of the number of particles colliding with the boundary). The latter was to test the operation of the boundary in a simulation scenario, which almost always has particles.

For both test cases, only simulation of a device in cartesian geometry is shown for the sake of brevity and the fact that the solution to the potential of the circuit boundary is highly dependant on the geometry (as discussed in the previous subsection).

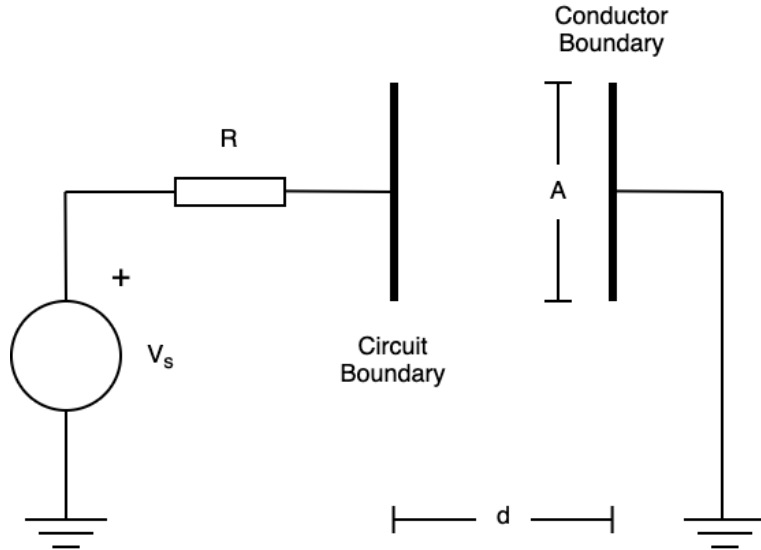


Figure B.4: Illustration of test case for Circuit boundary without particles.

### Test Case without Particles

An illustration of the device being simulated can be seen in figure B.4, where the Circuit boundary was placed along the  $y$ -axis at the left-most wall and a grounded *Conductor* boundary placed along the right-most wall. This device, without any particles, essentially behaves as a capacitor with a capacitance given by  $C = \frac{\epsilon_0 A}{d}$ . The parameters for this test case can be found in table B.3

Table B.3: Parameters for test case of Circuit boundary without particles.

Parameters	Values
$V_s$	1000 V
$R$	1000 $\Omega$
$A$	0.05 $m^2$
$d$	0.05 m
$C$	8.85 pF

Thus, this simulation models the charging of a capacitor in an  $RC$  circuit, which can be expressed as:

$$V_c = V_s(1 - e^{-t/\tau}) \quad (\text{B.17})$$

where the time constant is  $\tau = RC$ .

For the simulated device,  $C = 8.85$  pF and  $\tau = 8.85$  ns. From this, an analytical solution can

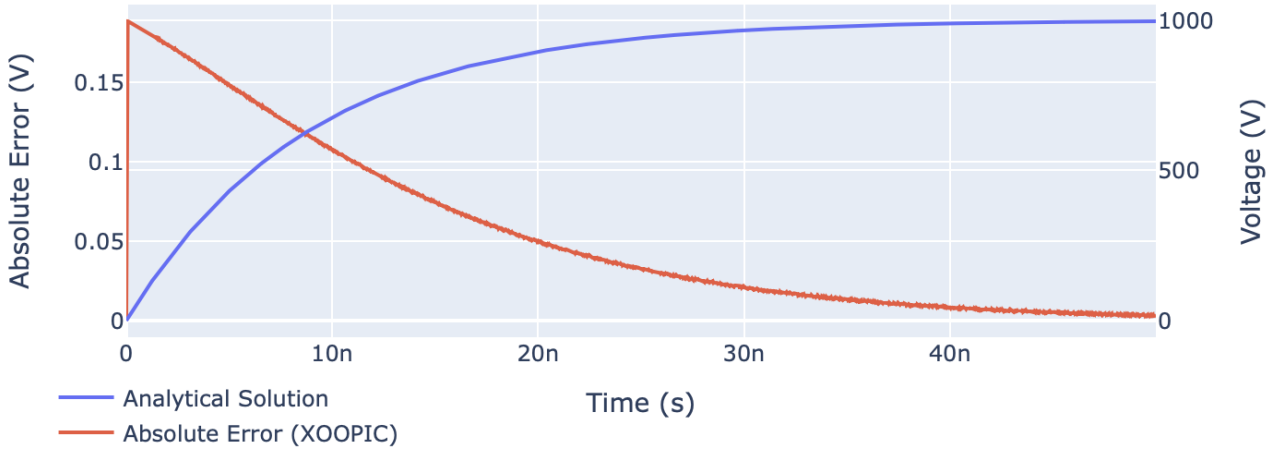


Figure B.5: Comparison between the analytical solution and XOOPIIC, where  $\Delta t = 10$  ps.

be determined, with the RC curve shown in figure B.5. For the XOOPIIC simulation, a run was performed from  $t = 0$  to  $t = 50$  ns (approximately 5 time constants), with a time step of  $\Delta t = 10$  ps. The resulting RC curve overlapped the one produced by the analytical solution, hence only the absolute error is shown.

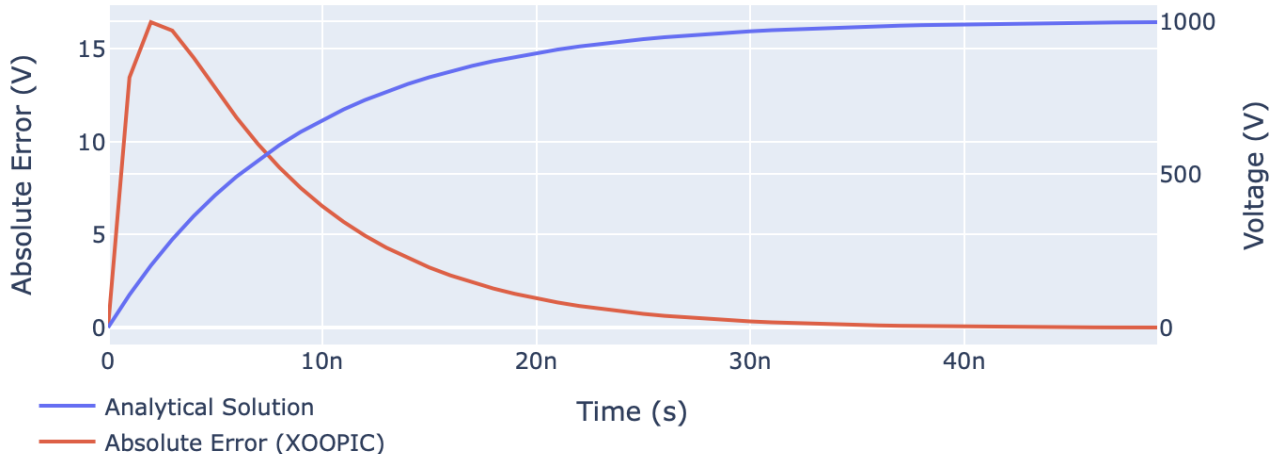


Figure B.6: Comparison between the analytical solution and XOOPIIC, where  $\Delta t = 1$  ns.

This error seen is a convergence error, which is due to the conduction charge values requiring a finite number of iterations before they converge to the true value. To illustrate this, the same simulation is run with a larger time step of  $\Delta t = 1$  ns (100 times that of the original simulation). These results can be seen in figure B.6. Notice that there is a significantly larger absolute error (nearly 100 times greater). However when observing the percentage error, seen in figure B.7, the differences are quite comparable. Therefore, so long as the time step used is sufficiently small (to ensure a small absolute error), the simulations can be said to be accurate

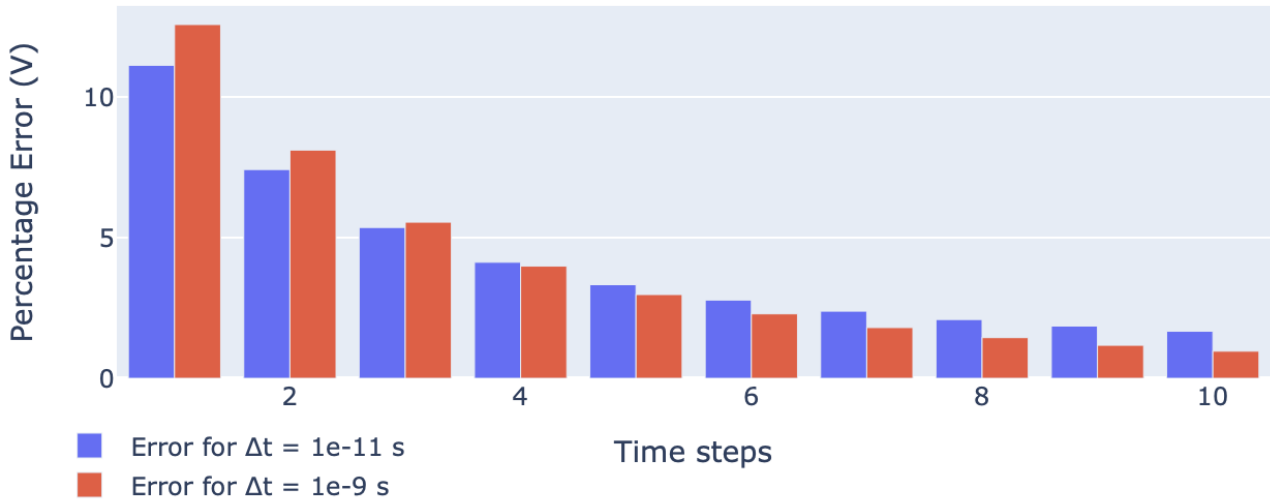


Figure B.7: Comparison of the error from XOOPIIC when  $\Delta t = 10$  ps and  $\Delta t = 1$  ns.

enough.

### Test Case with Particles

Generating a simplified test case to only asses the impact of particles on the Circuit boundary was slightly more challenging. The simulated circuit for this test case can be seen in figure B.8. As for the parameters used, they can be found in table B.4.

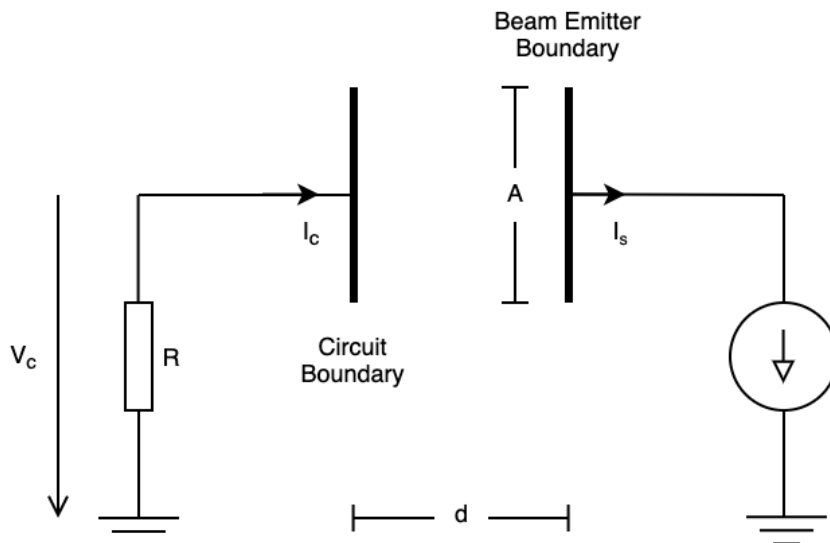


Figure B.8: Illustration of test case for Circuit boundary without particles.

Notice that the grounded Conductor boundary was replaced with a *Beam Emitter* boundary. The Beam Emitter is similar to the Current Source boundary, wherein a steady supply of charge

Table B.4: Parameters for test case of Circuit boundary with particles.

Parameters	Values
$V_s$	0 V
$I_s$	1 A
$R$	1000 $\Omega$
$A$	$5 \times 10^{-4}$ m $^2$
$d$	$5 \times 10^{-4}$ m
$C$	8.85 pF
$v_{d,x}$	1000 eV
$v_{d,y}$	0 eV

is supplied to the boundary. However, unlike the Current Source which simply deposits the charge at the boundary (which in turn generates a potential), the Beam Emitter releases this charge into the simulation domain in the form of particles. This steady source of particles is what enabled the evaluation of this test case. The particles emitted out of the Beam Emitter (i.e. towards the LHS) in this case were electrons, hence why source current  $I_s$  is shown in the opposite direction. To ensure no particle losses, collisions by the MCC were turned off, the simulated device was set to a vacuum, and the drift velocity of the particles along the  $y$ -axis,  $v_{d,y}$  was set to 0 eV.

As for the Circuit boundary itself, the source voltage  $V_s$  was grounded, implying that the potential of the boundary is solely given by the current through the resistor,  $I_c$ . Additionally, because the source current must be equal to the circuit current (as there were no losses) and one end of the resistor was grounded, the potential at the Circuit boundary has to be negative.

The analytical solution for this test case is given by the conduction current from electrons colliding with the Circuit boundary, and the displacement current across the capacitor. The conduction current is merely a step from 0 A to the  $-1$  A specified by the source current. It is negative because the current is leaving the boundary. The time at which this step occurs is given by the time taken for the electrons to travel across the device. As the drift velocity of the electrons along the direction of the  $x$ -axis was set to  $v_{d,x} = 1000$  eV, thus its true velocity can be determined using the equation for kinetic energy:

$$E_{ke} = \frac{1}{2}mv^2 \quad (\text{B.18})$$

where  $1 \text{ eV} = 1.6 \times 10^{-19} \text{ J}$ .

This resulted in a velocity of approximately  $1.87 \times 10^7 \text{ ms}^{-1}$ , hence it crossed the length of the device in roughly 30 ps. Thus this is when the step in conduction current should occur.

As for the displacement current, this is given by:

$$I_{disp} = C \frac{dV}{dt} \quad (\text{B.19})$$

Combining this with the analytical solution of the RC circuit in equation B.17, gives the displacement current of:

$$I_{disp} = \frac{V_{ss}}{R} e^{-\frac{t}{\tau}} \quad (\text{B.20})$$

where  $V_{ss}$  is the potential difference across the capacitor when it reaches a steady state, which is given as  $V_{ss} = I_s R$ . The displacement current is in opposite the opposite direction to the conduction current, hence in this case it is positive. Similarly to the conduction current, the displacement current at the surface of the Circuit boundary would only occur after the electrons collide with the boundary itself.

The overall potential is obtained by combining the contributions of the conduction and displacement currents with the resistance of the circuit. This is expressed in the equation below, and is illustrated in figure B.9.

$$V_c = \begin{cases} 0 & t < 30 \text{ ps} \\ I_s R (e^{-\frac{t}{\tau}} - 1) & t \geq 30 \text{ ps} \end{cases} \quad (\text{B.21})$$

For the simulation, a similar overall device geometry was used to that of the previous test, however the gap distance  $d$  was decreased to minimise the time required for the electrons to collide with the boundary. This meant that the area of the boundary plates  $A$  also had to be decreased to ensure that the capacitance, and by extension the time constant, remained the same. Again, the simulations were run from  $t = 0$  to  $t = 50$  ns, with a time step of  $\Delta t = 10$  ps. Figure B.9 also shows the absolute error of the Circuit boundary of the simulation as apposed

to that of the analytical solution. The error observed is much larger with a maximum error of approximately 26 V; quite a significant error. However, at the time of writing this report, the origin of this error is still unknown.

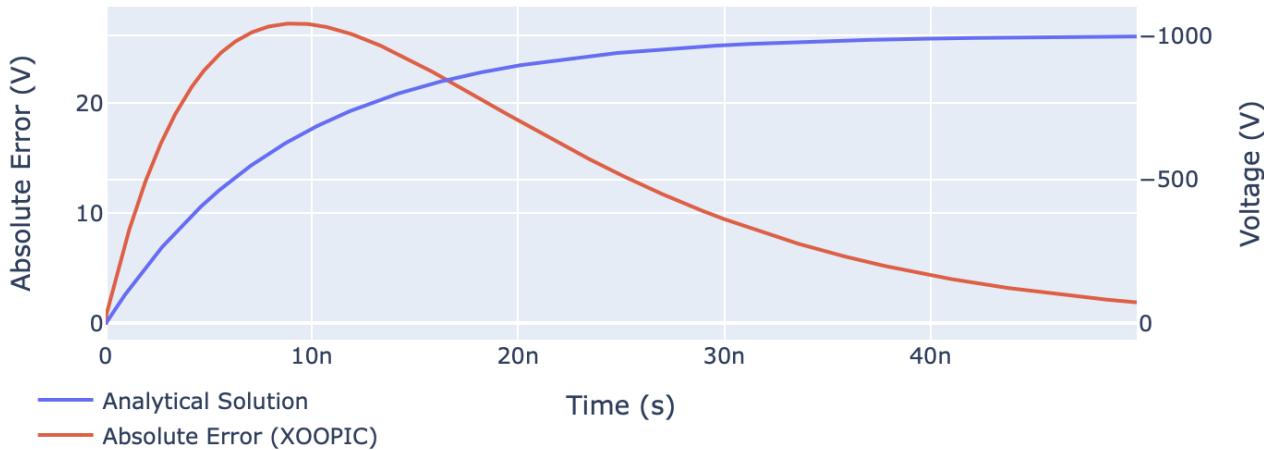


Figure B.9: Illustration of test case for Circuit boundary without particles.

#### B.2.4 Future Work

Aside from the Circuit boundary simulating a more accurate “real world” voltage source, it can possibly be used in model more complicated circuit networks. This is because, Thevenin’s theorem dictates that any linear circuit network can be represented by an equivalent circuit that contains a voltage source with a series impedance (which is a resistance in this case).

Nonetheless, most circuits also contain some amount of capacitance and/or inductance. Hence, it could potentially be beneficial to add a series inductor and capacitor to the Circuit boundary in addition to the existing resistor. To achieve this, the the RHS of Kirchoff’s voltage law, equation B.11, needs to be modified to include the potential due to the inductor,  $V = \frac{d^2Q}{dt^2}L$ , and the potential due to a capacitor,  $V = \frac{Q}{C}$ . This new equation can be rearranged to solve for the current conduction charge. From there, the same process can be applied to determine the potential of the Circuit boundary.

# Bibliography

- [1] IPCC, “Climate change: a threat to human wellbeing and health of the planet. taking action now can secure our future — IPCC,” Feb 2022.
- [2] “Inventory of u.s. greenhouse gas emissions and sinks — US EPA, url=<https://www.epa.gov/ghgemissions/inventory-us-greenhouse-gas-emissions-and-sinks>, journal=US EPA, author=EPA, year=2019, month=Apr.”
- [3] H. Ritchie and M. Roser, “CO<sub>2</sub> and greenhouse gas emissions,” *Our World in Data*, May 2020.
- [4] M. B. Ross, P. De Luna, Y. Li, C.-T. Dinh, D. Kim, P. Yang, and E. H. Sargent, “Designing materials for electrochemical carbon dioxide recycling,” *Nature Catalysis*, vol. 2, p. 648–658, Jul 2019.
- [5] U. Arnold, T. Brück, A. De Palmenaer, and K. Kuse, “Carbon capture and sustainable utilization by algal polyacrylonitrile fiber production: Process design, techno-economic analysis, and climate related aspects,” *Industrial and Engineering Chemistry Research*, vol. 57, p. 7922–7933, May 2018.
- [6] M. A. Lieberman and A. J. Lichtenberg, *Principles of Plasma Discharges and Materials Processing: Second Edition*. Wiley-Interscience, 2005.
- [7] J. T. Gudmundsson and A. Hecimovic, “Foundations of DC plasma sources,” vol. 26, p. 123001, nov 2017.
- [8] C. F. Gallo, “Coronas and Gas Discharges in Electrophotography:A Review,” *IEEE Transactions on Industry Applications*, vol. IA-11, no. 6, pp. 739–748, 1975.

- [9] A. Bogaerts, E. Neyts, R. Gijbels, and J. Van der Mullen, “Gas discharge plasmas and their applications,” *Spectrochimica Acta Part B: Atomic Spectroscopy*, vol. 57, pp. 609–658, apr 2002.
- [10] J. C. Eijkel, H. Stoeri, and A. Manz, “A molecular emission detector on a chip employing a direct current microplasma,” *Analytical Chemistry*, vol. 71, pp. 2600–2606, jul 1999.
- [11] M. Ueda, L. A. Berni, G. F. Gomes, A. F. Beloto, E. Abramof, and H. Reuther, “Application of a dc glow discharge source with controlled plasma potential in plasma immersion ion implantation,” *Journal of Applied Physics*, vol. 86, pp. 4821–4824, oct 1999.
- [12] K. H. Becker, K. H. Schoenbach, and J. G. Eden, “Microplasmas and applications,” *Journal of Physics D: Applied Physics*, vol. 39, p. R55, jan 2006.
- [13] R. R. Arslanbekov, A. A. Kudryavtsev, and R. C. Tobin, “On the hollow-cathode effect: Conventional and modified geometry,” *Plasma Sources Science and Technology*, vol. 7, pp. 310–322, aug 1998.
- [14] A. Watson and J. W. Gewartewski, *Principles of Electron tubes*. Van Nostrand, 1965.
- [15] F. Iza, G. J. Kim, S. M. Lee, J. K. Lee, J. L. Walsh, Y. T. Zhang, and M. G. Kong, “Microplasmas: Sources, Particle Kinetics, and Biomedical Applications,” *Plasma Processes and Polymers*, vol. 5, pp. 322–344, jun 2008.
- [16] V. I. Kolobov and A. S. Metel, “Glow discharges with electrostatic confinement of fast electrons,” vol. 48, p. 233001, may 2015.
- [17] H. Eichhorn, K. H. Schoenbach, and T. Tessnow, “Paschen’s law for a hollow cathode discharge,” *Applied Physics Letters*, vol. 63, pp. 2481–2483, aug 1993.
- [18] M. E. Pillow, “A critical review of spectral and related physical properties of the hollow cathode discharge,” *Spectrochimica Acta Part B: Atomic Spectroscopy*, vol. 36, pp. 821–843, jan 1981.

- [19] S. Y. Kornilov, I. V. Osipov, and N. G. Rempe, "Generation of narrow focused beams in a plasma-cathode electron gun," *Instruments and Experimental Techniques 2009* 52:3, vol. 52, pp. 406–411, jun 2009.
- [20] I. Yu Bakeev, A. S. Klimov, E. M. Oks, and A. A. Zenin, "Generation of high-power-density electron beams by a forevacuum-pressure plasma-cathode electron source," *Plasma Sources Science and Technology*, vol. 27, p. 075002, jul 2018.
- [21] D. M. Goebel, G. Becatti, I. G. Mikellides, and A. Lopez Ortega, "Plasma hollow cathodes," *Journal of Applied Physics*, vol. 130, p. 050902, aug 2021.
- [22] P. Chabert and N. Braithwaite, *Physics of radio-frequency plasmas*, vol. 9780521763. Cambridge University Press, jan 2011.
- [23] T. D. Chu, "High Frequency Breakdown Voltage," Tech. Rep. March, Superconducting Super Collider Project Office, mar 1992.
- [24] J. Pim, "The electrical breakdown strength of air at ultra-high frequencies," *Proceedings of the IEE - Part III: Radio and Communication Engineering*, vol. 96, pp. 117–129, mar 1949.
- [25] S. Sharma, N. Sirse, A. Kuley, and M. M. Turner, "Electric field nonlinearity in very high frequency capacitive discharges at constant electron plasma frequency," *Plasma Sources Science and Technology*, vol. 29, p. 045003, mar 2020.
- [26] Y. Ohtsu, "Physics of High-Density Radio Frequency Capacitively Coupled Plasma with Various Electrodes and Its Applications," *Plasma Science and Technology - Basic Fundamentals and Modern Applications*, nov 2018.
- [27] "Ccp reactor for semiconductor materials processing," May 2017.
- [28] K. Denpoh, "Effects of driving frequency on plasma density in Ar and H<sub>2</sub>/Ar capacitively coupled plasmas at Torr-order pressure," *Japanese Journal of Applied Physics*, vol. 60, p. 016002, dec 2021.

- [29] J. Lee and S. Hong, "Dual-frequency RF impedance matching circuits for semiconductor plasma etch equipment," *Electronics (Switzerland)*, vol. 10, p. 2074, aug 2021.
- [30] N. Yu, R. Jourdain, M. Gourma, F. Xu, A. Bennett, and F. Fang, "Power Dissipation of an Inductively Coupled Plasma Torch under E Mode Dominated Regime," *Micromachines 2021, Vol. 12, Page 834*, vol. 12, p. 834, jul 2021.
- [31] Y. Sakamoto, S. Maeno, N. Tsubouchi, T. Kasuya, and M. Wada, "Comparison of plasma parameters in ccp and icp processes appropriate for carbon nanotube growth," 2009.
- [32] J. Hopwood and F. Iza, "Ultrahigh frequency microplasmas from 1 pascal to 1 atmosphere," *Journal of Analytical Atomic Spectrometry*, vol. 19, pp. 1145–1150, sep 2004.
- [33] F. Krüger, M. J. Kushner, S. Shim, H. Lee, and S.-K. Nam, "Icp vs ccp in high aspect ratio etching of sio2 using ar/c4f8/o2 gas mixtures," in *2020 IEEE International Conference on Plasma Science (ICOPS)*, pp. 88–88, 2020.
- [34] U. Kogelschatz, "Dielectric-barrier discharges: Their History, Discharge Physics, and Industrial Applications," *Plasma Chemistry and Plasma Processing*, vol. 23, pp. 1–46, mar 2003.
- [35] S. J. Tingay, D. L. Kaplan, E. Lenc, K. M. J Alards, P. J. Bruggeman -, C. Constans, P. Mateo, R. Bazinette, R. Subileau, J. Paillol, and F. Massines, "Identification of the different diffuse dielectric barrier discharges obtained between 50 kHz to 9 MHz in Ar/NH3 at atmospheric pressure," *Plasma Sources Science and Technology*, vol. 23, p. 035008, may 2014.
- [36] R. Brandenburg, "Dielectric barrier discharges: progress on plasma sources and on the understanding of regimes and single filaments," *Plasma Sources Science and Technology*, vol. 26, p. 053001, apr 2017.
- [37] H. Toyoda, "Microwave plasma," in *RF Power Semiconductor Generator Application in Heating and Energy Utilization*, pp. 181–194, Springer Singapore, jan 2020.

- [38] J. Pollak, M. Moisan, and Z. Zakrzewski, “Long and uniform plasma columns generated by linear field-applicators based on stripline technology,” *Plasma Sources Science and Technology*, vol. 16, p. 310, mar 2007.
- [39] F. Iza and J. A. Hopwood, “Low-power microwave plasma source based on a microstrip split-ring resonator,” *IEEE Transactions on Plasma Science*, vol. 31, no. 4 I, pp. 782–787, 2003.
- [40] M. Surendra and D. B. Graves, “Capacitively coupled glow discharges at frequencies above 13.56 MHz,” *Applied Physics Letters*, vol. 59, p. 2091, jun 1998.
- [41] S. Rayne, “Thermal carbon dioxide splitting: A summary of the peer-reviewed scientific literature,” *Nature Precedings*, Apr 2008.
- [42] Z. Jiang, T. Xiao, V. L. Kuznetsov, and P. P. Edwards, “Turning carbon dioxide into fuel,” *Philosophical Transactions of the Royal Society A: Mathematical, Physical and Engineering Sciences*, vol. 368, p. 3343–3364, Jul 2010.
- [43] R. Snoeckx and A. Bogaerts, “Plasma technology-a novel solution for CO<sub>2</sub> conversion?,” oct 2017.
- [44] D. Pakhare and J. Spivey, “A review of dry (co<sub>2</sub>) reforming of methane over noble metal catalysts,” *Chem. Soc. Rev.*, vol. 43, p. 7813–7837, Feb 2014.
- [45] 2011.
- [46] U. Kogelschatz, “Dielectric-barrier discharges: Their history, discharge physics, and industrial applications,” *Plasma Chemistry and Plasma Processing*, vol. 23, no. 1, p. 1–46, 2003.
- [47] L. F. Spencer and A. D. Gallimore, “Efficiency of co<sub>2</sub> dissociation in a radio-frequency discharge,” *Plasma Chemistry and Plasma Processing*, vol. 31, p. 79–89, Nov 2010.
- [48] H. Xu, M. Shaban, S. Wang, A. Alkayal, D. Liu, M. G. Kong, F. Plasser, B. R. Buckley, and F. Iza, “Oxygen harvesting from carbon dioxide: simultaneous epoxidation and CO formation,” *Chemical Science*, 2021.

- [49] Y. Gorbanev, J. Golda, V. S.-v. der Gathen, and A. Bogaerts, “Applications of the COST Plasma Jet: More than a Reference Standard,” *Plasma 2019, Vol. 2, Pages 316-327*, vol. 2, pp. 316–327, jul 2019.
- [50] R. A. Dextre and K. G. Xu, “Effect of the Split-Ring Resonator Width on the Microwave Microplasma Properties,” *IEEE Transactions on Plasma Science*, vol. 45, pp. 215–222, feb 2017.
- [51] F. Iza and J. A. Hopwood, “Split-ring resonator microplasma: Microwave model, plasma impedance and power efficiency,” *Plasma Sources Science and Technology*, vol. 14, pp. 397–406, may 2005.
- [52] H. Wheeler, “Transmission-line properties of a strip on a dielectric sheet on a plane,” *IEEE Transactions on Microwave Theory and Techniques*, vol. 25, p. 631–647, Aug 1977.
- [53] J. P. Verboncoeur, A. B. Langdon, and N. T. Gladd, “An object-oriented electromagnetic PIC code,” *Computer Physics Communications*, vol. 87, pp. 199–211, may 1995.
- [54] H. C. Kim, F. Iza, S. S. Yang, M. Radmilović-Radjenović, and J. K. Lee, “Particle and fluid simulations of low-temperature plasma discharges: benchmarks and kinetic effects,” *Journal of Physics D: Applied Physics*, vol. 38, p. R283, sep 2005.
- [55] D. Tskhakaya, K. Matyash, R. Schneider, and F. Taccogna, “The Particle-In-Cell Method,” *Contributions to Plasma Physics*, vol. 47, pp. 563–594, dec 2007.
- [56] C. K. Birdsall, “Particle-in-Cell Charged-Particle Simulations, Plus Monte Carlo Collisions With Neutral Atoms, PIC-MCC,” *IEEE Transactions on Plasma Science*, vol. 19, no. 2, pp. 65–85, 1991.
- [57] R. Hockney and J. Eastwood, *Computer Simulation Using Particles*. CRC Press, mar 1988.
- [58] A. T. Gisbert and N. Piovella, “Multimode collective atomic recoil lasing in free space,” *Atoms*, vol. 8, p. 93, Dec 2020.

- [59] C. K. Birdsall and A. B. Langdon, *Plasma physics via computer simulation*. CRC Press, 1st ed ed., oct 2004.
- [60] W. H. Press, B. P. Flannery, S. A. Teukolsky, and W. T. Vetterling, *Numerical Recipes in C: The Art of Scientific Computing*. Cambridge University Press, 1988.
- [61] S. V.-U. Ha, T.-A. Vu, and H. M. Tran, “An Extended Occlusion Detection Approach for Video Processing,” *REV Journal on Electronics and Communications*, vol. 8, jan 2019.
- [62] W. H. Press, B. P. Flannery, S. A. Teukolsky, and W. T. Vetterling, *Numerical Recipes in C: The Art of Scientific Computing*. Cambridge University Press, 1988.
- [63] F. Wermelinger, “Diffusion with Alternating Direction Implicit (ADI) and Particle Strength Exchange (PSE) methods.”
- [64] W. H. Press, B. P. Flannery, S. A. Teukolsky, and W. T. Vetterling, *Numerical Recipes in C: The Art of Scientific Computing*. Cambridge University Press, 1988.
- [65] F. Iza, S. H. Lee, and J. K. Lee, “Computer modeling of low-temperature plasmas,” *Transworld Research Network*, vol. 37, no. 2, 2007.
- [66] V. Vahedi and M. Surendra, “A Monte Carlo collision model for the particle-in-cell method: applications to argon and oxygen discharges,” *Computer Physics Communications*, vol. 87, pp. 179–198, may 1995.
- [67] D. Tskhakaya, K. Matyash, R. Schneider, and F. Taccogna, “The particle-in-cell method,” *Contributions to Plasma Physics*, vol. 47, p. 563–594, Dec 2007.
- [68] J. P. Verboncoeur, M. V. Alves, V. Vahedi, and C. K. Birdsall, “Simultaneous Potential and Circuit Solution for 1D Bounded Plasma Particle Simulation Codes,” *Journal of Computational Physics*, vol. 104, pp. 321–328, feb 1993.
- [69] V. Vahedi and G. Dipeso, “Simultaneous Potential and Circuit Solution for Two-Dimensional Bounded Plasma Simulation Codes,” *Journal of Computational Physics*, vol. 131, pp. 149–163, feb 1997.